

POLITECNICO DI TORINO

Master's degree course
in Mathematical Engineering

Master's degree Thesis

**A non local model for 2D cell migration
in response to mechanical stimuli**



Supervisors

Prof.ssa Chiara Giverso
Prof. Luigi Preziosi

Candidate

Roberto Marchello
s277438

Academic Year 2021-2022

Summary

Cell migration is one of the most important and most studied phenomena in biology and plays a fundamental role for many physiological and pathological processes such as morphogenesis, wound healing and tumorigenesis. Understanding cell migration, considering the stimuli and mechanisms involved, can also help in the development of new therapeutic approaches. In this respect, a model that can reproduce experimental observations as closely as possible is of undoubted utility for medical and bioengineering purposes.

In the body many cells, such as fibroblasts, immune cells and some types of cancer cells, migrate individually by adhering to a protein substrate known as the extracellular matrix (ECM). There are many mechanisms affecting cell motion. For instance, it is well known that cells sense the concentration gradients of particular chemicals and migrate attracted or repelled by them (*chemotaxis*). In recent years, researchers have performed experiments demonstrating that cells can also migrate in response to mechanical stimuli of the substrate to which they adhere: motion toward regions of the substrate with higher stiffness is called *durotaxis*, while motion guided by the stress or the deformation of the substrate itself is called *tensotaxis*. Unlike chemotaxis, these migratory processes are not yet fully understood from a biological point of view, which makes the investigation of mathematical models suitable for their reproduction even more important.

This Thesis is placed exactly in this context. In fact, its goal is to appropriately modify a mathematical model proposed by Colombi et al. in [1], that deals with single-cell migration in response to chemotactic signals, to account for mechanical stimuli and thus to be able to model and simulate the phenomena of durotaxis and tensotaxis, for example as reported in [2]. In the case of durotaxis the cell moves by changing its direction of polarization and its motility according to the different stiffness of the substrate and the amount of ECM, respectively. In the case of tensotaxis, the substrate on which the cell moves is appropriately deformed and the cell polarizes and migrates in response to proper scalar measures of the substrate strain or stress.

From the mathematical point of view the equations of motion of the cell are nonlocal integro-differential equations, with integral terms that are in charge of describing the nonlocal evaluation of the considered mechanical cue by the cell in its neighbourhood. Their evaluation calls for explicit numerical methods, as well as appropriate quadrature techniques to account for possible singularities of the integrand functions (e.g. piecewise constant substrate stiffness). In addition, it must be taken into account that the integrand functions may be defined only pointwise, and therefore their interpolation at quadrature nodes is necessary. The equations are solved with a *MATLAB*[®] code by partitioning the bidimensional substrate with a uniform square mesh, eventually deformed in the case of tensotaxis.

The mechanical stimulus to be integrated in the equations of motion is known experimentally in the case of durotaxis, while it is derived by the solution of the mechanical

problem for the substrate in the case of tensotaxis. Specifically, the mass and momentum balance equations for the substrate are defined neglecting the mutual mechanical interaction between the cell and the substrate. The latter is modeled either as a linear elastic solid or as a hyperelastic Yeoh's solid. Then, the mechanical problem is solved with the software *COMSOL Multiphysics*[®] and the quantities of interest are imported into the *MATLAB*[®] code that numerically implements the equations of motion, taking into account that the deformation of the substrate implies a deformation of the mesh.

In both cases the equations of motion of the cell are solved by simulating different experimental setups found in the literature and the numerical simulations show a qualitative agreement with the experimental observations.

Sommario

La migrazione cellulare è uno dei fenomeni più importanti e più studiati in biologia. Esso gioca un ruolo fondamentale per molti processi fisiologici e patologici come la morfogenesi, la guarigione delle ferite e la tumorigenesi. La comprensione della migrazione cellulare, considerando gli stimoli e i meccanismi coinvolti, può inoltre aiutare nello sviluppo di nuovi approcci terapeutici. A questo proposito, un modello che possa riprodurre il più fedelmente possibile le osservazioni sperimentali è di indubbia utilità per scopi medici e bioingegneristici.

All'interno dell'organismo vi sono molte cellule, come i fibroblasti, le cellule immunitarie e alcuni tipi di cellule tumorali, che migrano individualmente aderendo a un substrato proteico noto come matrice extracellulare (ECM). Il movimento delle cellule è influenzato da molti meccanismi differenti. Ad esempio, è noto che le cellule percepiscono i gradienti di concentrazione di particolari sostanze chimiche e migrano attratte o respinte da esse (*chemiotassi*). Negli ultimi anni, i ricercatori hanno eseguito esperimenti che dimostrano che le cellule possono migrare anche in risposta a stimoli meccanici del substrato a cui aderiscono: il movimento verso regioni del substrato con maggiore rigidità è chiamato *durotassi*, mentre il movimento guidato dallo stress o dalla deformazione del substrato stesso è chiamato *tenсотassi*. A differenza della chemiotassi, questi processi migratori non sono ancora pienamente compresi dal punto di vista biologico, il che rende ancora più importante lo studio di modelli matematici in grado di simularli.

Questa Tesi si colloca esattamente in questo contesto. Infatti, il suo obiettivo è quello di modificare opportunamente un modello matematico proposto da Colombi et al. in [1], che si occupa della migrazione di singole cellule in risposta a segnali chemiotattici, in modo da tener conto degli stimoli meccanici e poter così modellare e simulare i fenomeni di durotassi e tenсотassi, ad esempio come riportato in [2]. Nel caso della durotassi, la cellula si muove cambiando la sua direzione di polarizzazione e la sua motilità secondo la diversa rigidità del substrato e la quantità di ECM. Nel caso della tenсотassi, il substrato su cui la cellula si muove è opportunamente deformato e la cellula si polarizza e migra in risposta a delle misure scalari di deformazione o di stress del substrato stesso.

Dal punto di vista matematico, le equazioni del moto della cellula sono equazioni integro-differenziali non locali, con termini integrali che hanno il compito di descrivere la valutazione non locale da parte della cellula degli stimoli meccanici considerati. La loro valutazione richiede metodi numerici di avanzamento in tempo espliciti, così come tecniche di quadratura appropriate per tenere conto di eventuali singolarità delle funzioni integrande (ad esempio, rigidità del substrato costante a tratti). Inoltre, si deve tener

conto del fatto che le funzioni integrande possano non essere definite analiticamente ma solo in alcuni punti del dominio, e quindi è necessaria la loro interpolazione nei nodi di quadratura. Le equazioni sono risolte tramite un codice *MATLAB*[®] partizionando il substrato bidimensionale attraverso una mesh quadrata uniforme, eventualmente deformata nel caso della tensotassi.

Lo stimolo meccanico da integrare nelle equazioni del moto è noto sperimentalmente nel caso della durotassi, mentre è ricavato dalla soluzione del problema meccanico per il substrato nel caso della tensotassi. In particolare, definiamo le equazioni di equilibrio della massa e della quantità di moto per il substrato, trascurando l'interazione meccanica reciproca tra la cellula e il substrato stesso. Quest'ultimo è modellato come un solido elastico lineare o come un solido iperelastico di Yeoh. Poi il problema meccanico viene risolto con il software *COMSOL Multiphysics*[®] e le quantità di interesse vengono importate nel codice *MATLAB*[®] che implementa numericamente le equazioni del moto, tenendo conto che la deformazione del substrato implica una deformazione della mesh.

In entrambi i casi le equazioni del moto della cellula sono risolte simulando diversi setup sperimentali presenti in letteratura, e le simulazioni numeriche effettuate forniscono risultati qualitativamente in accordo con quelli sperimentali.

Ringraziamenti

Giunto al termine di questo percorso, vorrei ringraziare chi ha contribuito alla stesura di questo lavoro e soprattutto chi mi è stato accanto in questi ultimi anni.

Vorrei innanzitutto ringraziare i miei relatori, la Prof.ssa Chiara Givero e il Prof. Luigi Preziosi, per il tempo, l'aiuto e il supporto che mi hanno dato in questi ultimi mesi, e per avermi incuriosito e appassionato con le loro tematiche di ricerca. Un sentito grazie anche alla Dott.ssa Annachiara Colombi per avermi presentato il modello matematico da cui il mio lavoro trae spunto e per aver condiviso il codice risolutivo di partenza. Un ringraziamento anche alle Prof.sse Silvia Falletta e Letizia Scuderi per alcuni utili consigli sull'implementazione numerica del modello.

Un grazie a tutti i Professori e le Professoressa che, nel bene e nel male, mi hanno insegnato qualcosa non solo dal punto di vista accademico, e hanno fatto parte di questo mio percorso. In particolare un ringraziamento al Prof. Marco Morandotti per tutti i consigli e per avermi introdotto al mondo della ricerca, che spero possa essere il mio futuro.

Grazie a quei pochi colleghi (e amici!) che hanno condiviso con me le lezioni più interessanti e le più noiose, i pranzi in mensa, i lavori di gruppo e i caffè, con il rammarico che negli ultimi due anni ci siamo potuti vedere quasi sempre solo di fronte a uno schermo.

Grazie alla mia famiglia per esserci sempre stata, e sono sicuro che non smetterà mai di farlo. Grazie ai miei genitori, ai miei fratelli, a tutti i cugini e le cugine, zii e zie, nonni e nonne, anche a chi non potrà leggere questi ringraziamenti. Ognuno di voi ha contribuito in maniera unica al mio percorso di crescita, e avrà sempre un posto nel mio cuore.

Grazie ai miei amici, ormai sparsi un po' in tutta Italia e non solo, a chi conosco da una vita e a chi solo da poco, ai più distanti e ai più vicini. Grazie per tutti i momenti passati insieme, le risate, le mangiate e le riflessioni più profonde.

Infine, il mio ringraziamento più grande va a te, Chiara. Grazie per essere sempre al mio fianco nei momenti di gioia e in quelli più bui, grazie per amare ogni parte di me con tutta te stessa, grazie per condividere con me ogni tua emozione. Questa Tesi è dedicata a te, la mia ragazza e la mia migliore amica. Questo non è un punto, ma solo l'inizio di una nuova avventura. E sono sicuro che, in un modo o nell'altro, tu sarai con me.

Roberto Marchello, Torino, 07/03/2022

Contents

List of Tables	9
List of Figures	10
1 Introduction	15
1.1 Biological background	15
1.1.1 How cells migrate	15
1.1.2 Cell movement is guided by the rigidity of the substrate: durotaxis	17
1.1.3 Cell migration due to substrate strains and stresses: tensotaxis . . .	18
1.2 Mathematical modeling background	20
1.3 Aim and structure of the Thesis	23
2 The mathematical model	25
2.1 The model for cell migration	25
2.2 Substrate mechanics	28
2.2.1 Finite deformations	29
2.2.2 Small deformations	34
2.2.3 Plane stress approximation	35
3 Numerical implementation	37
3.1 Mechanical manipulation of the substrate	37
3.2 Time-integration for the cell migration model	39
3.2.1 Explicit Runge-Kutta methods	41
3.2.2 Tailored Gauss-Legendre quadrature formula	42
3.2.3 Interpolation methods	44
4 Numerical simulations	47
4.1 Parameters and kernels K_r and K_θ	47
4.2 Validation and choice of the numerical methods	49
4.2.1 Addition of a random term in cell direction	53
4.3 Durotaxis	53
4.3.1 Piecewise constant rigidity	55
4.3.2 Regular smooth rigidity	55
4.4 Tensotaxis	60

4.4.1	Differences in substrate's mechanical behaviour	62
4.4.2	Pulling or pushing the substrate	64
5	Conclusions and perspectives	69
	Bibliography	71

List of Tables

1.1	Summary table with the models for cell migration due to mechanical stimuli reviewed in Section 1.2.	22
4.1	Relative error $\text{err}_{\mathbf{x}}^{N,\Delta}$ defined in Eq. (4.8) and estimated order of convergence EOC^Δ given in Eq. (4.9) for the solution of the benchmark test defined in Section 4.2 obtained with Euler method coupled with a linear interpolation.	51
4.2	Relative error $\text{err}_{\mathbf{x}}^{N,\Delta}$ defined in Eq. (4.8) and estimated order of convergence EOC^Δ given in Eq. (4.9) for the solution of the benchmark test defined in Section 4.2 obtained with Euler method coupled with a natural neighbor interpolation.	51
4.3	Relative error $\text{err}_{\mathbf{x}}^{N,\Delta}$ defined in Eq. (4.8) and estimated order of convergence EOC^Δ given in Eq. (4.9) for the solution of the benchmark test defined in Section 4.2 obtained with Heun method coupled with a linear interpolation.	52
4.4	Relative error $\text{err}_{\mathbf{x}}^{N,\Delta}$ defined in Eq. (4.8) and estimated order of convergence EOC^Δ given in Eq. (4.9) for the solution of the benchmark test defined in Section 4.2 obtained with Heun method coupled with a natural neighbor interpolation.	52
4.5	Means and standard deviations of the values of the constants c_1 and c_3 in Eq. (3.3) and E in Eq. (4.26), identified in [4] when fitting measurements on polyacrylamide gels (PAG) made with 10% of acrylamide and varying concentrations of bis-acrylamide [<i>Bis</i>].	62
4.6	Maximum values of first principal invariant of stress, displacement magnitude and first principal strain (that is the trace of \mathbb{E}), referring to the results of Fig. 4.14.	64
4.7	Maximum values of first principal invariant of stress, displacement magnitude and first principal strain, referring to the same problem of Fig. 4.14, but considering $f_b = 15.7$ kPa.	64

List of Figures

1.1	The cycle of cell migration, from top to bottom. i) Cell attaches to the substratum. ii) Polarized cell produces a protrusion in form of a lamellipodium at the leading edge. iii) Strong focal contacts arise in the front while the cortex is under tension and the rear contracts. The adhesion in the rear detaches thereby the cell moves forward. iv) A new forward directed protrusion is formed to start the next cycle. From [29].	16
1.2	Figure showing experiments by Lo et al. [2] in which cells are seeded on a matrix with two different stiffnesses. Panel (a) shows a cell that is placed on the softer side of the matrix and then over time migrates onto the stiffer side. Panel (b) shows a cell that is placed on the stiffer side of the matrix initially and over time moves toward the discontinuity, but then stays on the stiffer side.	18
1.3	The cell forms protrusions (cyan) and it experiences a stiffer substrate on the right, so forces develop much faster on the right, allowing FAs to stabilize there. At the left, FAs fail to stabilize, allowing the cell to retract in order to propel itself forward and generate new FAs at the front. This continues and the cell moves to the right. Adapted from [8].	19
1.4	Figure showing experiments by Lo et al. [2] in which the substrate is stretched with a blunted microneedle. In panel (a) the needle was inserted near the rear part of a cell that was migrating away from it. The needle was then moved away from the cell, which changed its polarization and moved toward the needle. In panel (b) the needle was inserted near the front end of a cell that was migrating toward it. The needle was then moved toward the cell, which changed its polarization and moved away from the needle. The direction of movement of the microneedle is indicated by an arrow, and regions of lamellipodia development are indicated by arrowheads. . . .	20
2.1	On the left, cell polarization process (i.e. the actual polarization \mathbf{w} and the preferred axis \mathbf{W}) is regulated only by the spatial distribution of the quantity c (see the orange shadow) within the cell sensing region $\mathcal{S}(\mathbf{x}_p(t))$ (see the blue circle), as perceived by the individual according to the weight function K (see the green shadow). On the right, cell intrinsic motility (i.e. the actual speed $v(t)$) depends only on the spatial distribution m non-locally perceived at its leading front. Both figure are reproduced from [1]. .	28

3.1	The squared domain $\Omega = [0, L] \times [0, L]$ with a small circle \mathcal{D} in the center that models the manipulation with the needle ($\beta = \pi/2$ in Eq. 3.7) and with the boundary condition $\mathbf{u} = \mathbf{0}$ on $\partial\Omega$	38
3.2	Panel (a) shows an example of a triangular mesh for the domain Ω automatically generated by the software <i>COMSOL Multiphysics</i> [®] to solve the mechanical problem. Panel (b) shows an example of a $\Lambda \times \Lambda$ tensor grid with $\Lambda = 70$. Panel (c) shows the same grid of panel (b) when deformed as defined in Eq. (3.13).	39
3.3	Representative case where the distribution c is defined only over a finite amount of points (i.e. the orange dots) which do not coincide with the quadrature nodes (i.e. the blue dots) required to evaluate \mathbf{W} (from [1]).	40
3.4	On the left, a stress field in Lagrangian form (or plotted on the undeformed tensor grid as in panel (b) of Fig. 3.2, equivalently). On the right, the same stress field in Eulerian form (or plotted on the correspondent deformed grid as in panel (c) of Fig. 3.2, equivalently).	41
3.5	An example of quadrature nodes (blue, red, and green dots) used inside the sensing region $\mathcal{S}(\mathbf{x}_{pn})$ (blue circle) for the computation of \mathbf{W}_n if the field c is defined as in Eq. (3.22) and the cell senses the discontinuity to the right of its center.	43
3.6	The Voronoi tiles of a scattered point set $\{\mathbf{x}_1, \dots, \mathbf{x}_9\}$, within the addition of a new point \mathbf{x} (see Eqs. (3.28), (3.29), (3.30)). Bold lines indicate the new tile of point \mathbf{x} ; the dotted lines inside it show the old tile boundaries before the addition of point \mathbf{x} . The Delaunay triangles associated with the Voronoi tessellation are also shown, indicated by thin dashed lines; the triangle edges are perpendicular bisectors of the tile edges. Figure reproduced from [54].	45
4.1	Kernel K_r defined in Eq.(4.1) and used for the computation of cell preferred direction of motion in Eq. (3.10).	48
4.2	Different choices for the kernel K_θ used for the computation of cell preferred direction of motion in Eq. (3.10). The “unbiased kernel” defined in Eq. (4.4) is shown on the left for $k_1 \in \{1,2,4\}$, whereas the “biased kernel” defined in Eq. (4.3) is shown on the right.	49
4.3	Reference trajectory of a cell initially located at $\mathbf{x}_p(0) = (3/4L, L/4)$ (white circle) and with $\mathbf{w}(0) = (0,1)$ (red arrow), computed with $\bar{N} = 3200$ time-steps and $T = 16$ h. The fields c and m are defined in Eqs. (4.5) and (4.6), respectively, and the kernels K_r and K_θ in Eqs. (4.1) and (4.3), respectively. The colored symbols denote the position at the instants $T/4$ (yellow square), $T/2$ (red diamond), $3T/4$ (green circle).	50
4.4	Function f defined in Eq. (4.14) and used in Eq. (3.12) for the constitutive relation of cell motility.	54

4.5	Solution with initial conditions set in Eq. (4.18) (white circle and red arrow), computed with $N = 100$ time-steps and $T = 16$ h. The fields c (or E) and m are defined in Eqs. (4.16) and (4.17), respectively, and the kernels K_r and K_θ in Eqs. (4.1) and (4.3), respectively. The colored symbols denote the position at the instants $T/4$ (yellow square), $T/2$ (red diamond), $3T/4$ (green circle). On the left, the solution without the random term. On the right, the solution with the additional random term defined in Subsection 4.2.1.	56
4.6	10 different trajectories solutions of the problem set as on the right panel of Fig. 4.5.	56
4.7	10 different trajectories computed with $N = 200$ time-steps and $T = 32$ h. The fields c (or E) and m are defined in Eqs. (4.16) and (4.17), respectively, and the kernels K_r and K_θ in Eqs. (4.1) and (4.4), respectively. The white circles are the initial positions of the cell, that are always placed $50 \mu\text{m}$ from the stiffness discontinuity.	57
4.8	Solution with initial conditions set in Eq. (4.20) (white circle and red arrow), computed with $N = 100$ time-steps and $T = 16$ h. The field c (or E) is defined in Eq. (4.19), while we set $m = 0.5$ uniformly. The kernels K_r and K_θ are defined in Eqs. (4.1) and (4.3), respectively. The colored symbols denote the position at the instants $T/4$ (yellow square), $T/2$ (red diamond), $3T/4$ (green circle). On the left, the solution without the random term. On the right, the solution with the additional random term defined in Subsection 4.2.1.	58
4.9	10 different trajectories solutions of the problem set as on the right panel of Fig. 4.8.	58
4.10	Solution with initial conditions set in Eq. (4.20) (white circle and red arrow), computed with $N = 100$ time-steps and $T = 16$ h. The field c (or E) is defined in Eq. (4.19), while we set $m = 0.5$ uniformly. The kernels K_r and K_θ are defined in Eqs. (4.1) and (4.4), respectively. The colored symbols denote the position at the instants $T/4$ (yellow square), $T/2$ (red diamond), $3T/4$ (green circle). On the left, the solution without the random term. On the right, the solution with the additional random term defined in Subsection 4.2.1.	59
4.11	10 different trajectories solutions of the problem set as on the right panel of Fig. 4.10.	59
4.12	Qualitative differences between the substrate strain energy density (on the left) and its square root (on the right) in a representative case, in Lagrangian coordinates.	61
4.13	Function f defined in Eq. (4.23) for $v_{min} = 0.3V_{max}$ and used in Eq. (3.12) for the constitutive relation of cell motility.	61
4.14	Results from the mechanical problem of the substrate, with load in Eq. (3.7) identified by $f_b = 6.1 \text{ kPa}$, $\beta = \pi/2$, and being \mathcal{D} placed in the center of Ω and with radius $23.33 \mu\text{m}$. The left and right columns refer to a linear or non-linear response, respectively.	63

4.15	The square root of the strain energy density (on the left) and the first principal invariant of stress (on the right) of the substrate, i.e. the fields c and m , are plotted in Eulerian coordinates, for the mechanical problem discussed in Subsection 4.4.1, with $f_b = 6.1$ kPa.	65
4.16	Solution with initial conditions set in Eq. (4.27) (white circle and red arrow), computed with $N = 100$ time-steps and $T = 16$ h. The fields c and m are shown in Fig. 4.15. The kernels K_r and K_θ are defined in Eqs. (4.1) and (4.4), respectively. The colored symbols denote the position at the instants $T/4$ (yellow square), $T/2$ (red diamond), $3T/4$ (green circle). On the left, the solution without the random term. On the right, the solution with the additional random term defined in Subsection 4.2.1.	66
4.17	10 different trajectories solutions of the problem set as on the right panel of Fig. 4.16.	66
4.18	Solution with initial conditions set in Eq. (4.28) (white circle and red arrow), computed with $N = 200$ time-steps and $T = 32$ h. The fields c and m are shown in Fig. 4.15. The kernels K_r and K_θ are defined in Eqs. (4.1) and (4.4), respectively. The colored symbols denote the position at the instants $T/4$ (yellow square), $T/2$ (red diamond), $3T/4$ (green circle). On the left, the solution without the random term. On the right, the solution with the additional random term defined in Subsection 4.2.1.	67
4.19	10 different trajectories solutions of the problem set as on the right panel of Fig. 4.18.	67

Chapter 1

Introduction

Cell migration is a critical phenomenon occurring in several biological processes, such as morphogenesis, wound healing and tumorigenesis [35, 36]. Cell motility deficiency is associated with anomalies and complications that can compromise short-term or long-term health of individuals. Understanding cell migration as an integrated and coordinated process, considering the stimuli and mechanisms involved, may help in the development of the new therapeutic approaches to fight pathological processes [25]. For these reasons, research on cell migration has drawn the attention of the scientific community during the last decades; it has now become a leading interdisciplinary research field that calls for the collaboration of cellular biologists with experts from other disciplines, such as computer imaging, engineering, and mathematical modeling.

In this Chapter we will review the biological background needed to understand why and how cell migration occurs, mostly focusing on the motion driven by mechanical stimuli, and we will review some of the mathematical and computational models that have already provided insights into this complex process.

1.1 Biological background

1.1.1 How cells migrate

While some body cells are often in suspension (e.g. circulating cells in blood), most body cells need to attach to a polymer-like structure called the extracellular matrix (ECM) to function properly in a tissue. It has become clear that adherent cells anchor to a substrate and then exert contractile forces in order to explore the properties of their environment, which is a part of the so-called process of mechanosensing [22, 23]. More in detail, cell migration onto two dimensional (2D) substrates is conventionally described according to a cycle of four active phases [19, 28, 29, 39]:

1. the protrusion driven by polymerization of the branched actin network at the leading edge of the cell (the lamellipodium);
2. the adhesion to the substrate of the protruding part by engagement and disengagement of transmembrane adhesion molecules, mainly integrins;

3. the cytoskeleton contraction due to the activity of myosin motors;
4. the actin network depolymerization and tail detachment with consequent retraction at the cell rear.

These different steps of the migratory process are observed most distinctly in slow-moving cells, such as fibroblasts, and they are schematized in Fig. 1.1.

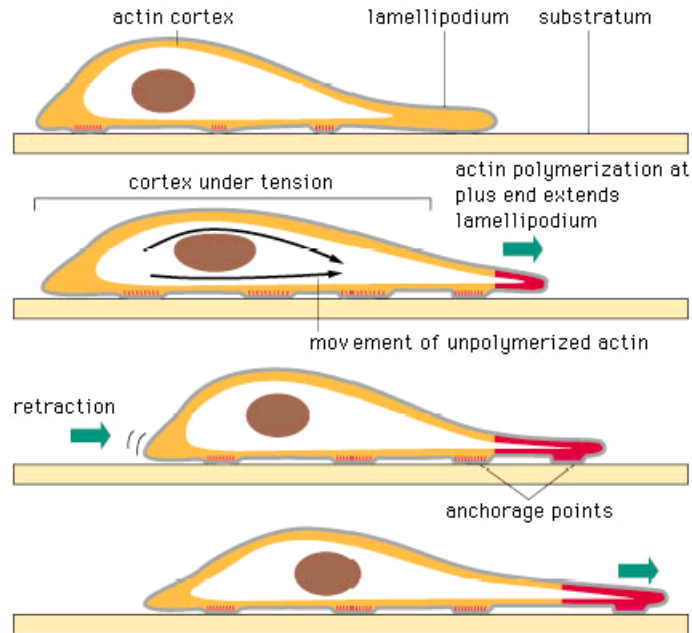


Figure 1.1: The cycle of cell migration, from top to bottom. i) Cell attaches to the substratum. ii) Polarized cell produces a protrusion in form of a lamellipodium at the leading edge. iii) Strong focal contacts arise in the front while the cortex is under tension and the rear contracts. The adhesion in the rear detaches thereby the cell moves forward. iv) A new forward directed protrusion is formed to start the next cycle. From [29].

While chemical processes are certainly at play, mechanical forces play a critical role in integrin-mediated adhesion and cellular responses [13, 23]. Integrins and focal adhesions (FAs) (a protein complex consisting of clustered integrins and other cytoplasmic molecules) mediate mechanical force transmission to the cytoskeleton, recruit cytoplasmic proteins and activate a cascade mechanism that leads from mechanical force to the alteration of cytoplasmic activities. Despite we focus on this integrin-mediated migration, it has been also showed that in three-dimensional (3D) confinement, migration is possible without the formation of integrin-based attachments, within the so called *adhesion-independent migration* [37, 38].

The initiation of the whole process that leads to cell migration requires a polarization of the cell in order to discriminate the leading edge from the trailing edge and implies a loss of symmetry from the stationary nonmoving configuration [17, 19].

Cell polarization can be either self-regulated, leading to a biased persistent random walk in the absence of external signals, or triggered by various stimuli, including diffusible chemical cues (chemotaxis [28, 40]), substrate-bound chemicals or cellular adhesion sites (haptotaxis [28, 41]), mechanical substrate compliance (durotaxis [2, 8]), mechanical strains on the substrate (tensotaxis [2, 22]), geometric features of the substrate (topotaxis [28, 42]), electric fields (galvanotaxis [28, 43]), gradients of light intensity (phototaxis [44, 45]), currents of fluids (rheotaxis [46, 47]). The external stimulus is converted into internal gradients of signaling molecules that guide the cytoskeleton mechanisms performing the motile response.

For the purpose of this Thesis, we will focus on cell movement driven by mechanical stimuli, i.e. durotaxis and tensotaxis. It is important to clarify that in the model we will develop we do not focus on the subcellular mechanisms involved in the migration, but we give a phenomenological description of them at the cellular scale. Therefore, the mechanisms of motion are treated separately even though they likely involve similar or analogous subcellular mechanisms.

1.1.2 Cell movement is guided by the rigidity of the substrate: durotaxis

One of the first experimental studies about the influence of mechanical stimuli on cell migration was developed by Lo et al. [2]. They evaluated the influence of the stiffness gradient on cellular locomotion and firstly termed *durotaxis* this rigidity-guided cell movement [3, 8–10, 13, 14, 18, 23, 24, 28, 31–33]. As shown in Fig. 1.2, fibroblasts were placed in the middle of a collagen-coated polyacrylamide substrate sheet, half of which was soft and the other half of which was stiff, under conditions such that the only way the cells can detect this stiffness discontinuity is by a process of active tactile exploration. The results showed that the cells either migrated onto the stiffer side when they are initially placed on the soft side or stayed on the stiffer side when they are seeded there. In doing so, they showed that fibroblasts tend to prefer stiff matrices to softer ones. Similar results have been obtained more recently in [14] for pancreatic cells.

It is still not completely understood which molecular mechanisms regulate such cellular response to ECM stiffness. Cells are able to sense matrix stiffness through integrins and FAs, that dynamically assemble and disassemble, at a rate that is regulated biochemically and mechanically. The disassembly rate is higher on soft ECMs and is lower on stiffer ECMs, so that FAs stabilize more easily on stiffer ECMs [8] (Fig. 1.3). The stronger mechanical feedback pull the cell towards the stiffer region and cause a bias in directional movement and have other consequences on cytoskeletal and focal adhesion organization [2].

It has been revealed that individual focal adhesions do not necessarily exert stable traction forces in response to unchanging ECM stiffness. In fact, while some individual focal adhesions may display stable traction forces, others exhibit tugging traction in the manner of a repeated cycle of tugging and release. Each focal adhesion acts autonomously and its stability do not depend on its neighbors. This tugging traction has been shown to be dispensable to other forms of cell migration, such as chemotaxis, but required for durotaxis. The FA proteins are required in order to exhibit high traction and tugging

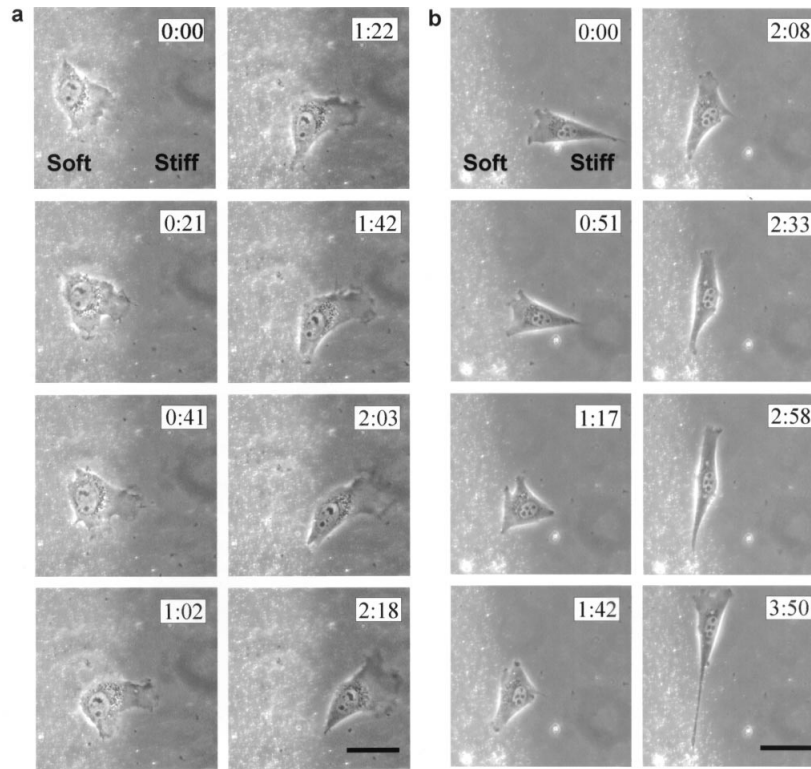


Figure 1.2: Figure showing experiments by Lo et al. [2] in which cells are seeded on a matrix with two different stiffnesses. Panel (a) shows a cell that is placed on the softer side of the matrix and then over time migrates onto the stiffer side. Panel (b) shows a cell that is placed on the stiffer side of the matrix initially and over time moves toward the discontinuity, but then stays on the stiffer side.

traction across a wide range of ECM rigidities. Furthermore, a reduction in FA tension by transferring cells to softer ECM results in a switching from stable to tugging states [13].

The mechanosensitive growth of FAs is key to our understanding of cellular responses to ECM stiffness, but how FAs and cytoskeletal force generation work together to regulate cell spreading, cell shape, and durotaxis is still to be elucidated [28].

1.1.3 Cell migration due to substrate strains and stresses: tensotaxis

Cells respond to external forces applied on the substrate by changing shape and direction of motion. When stresses are induced on the substrate a protrusion first and then the entire cell tend to move towards tensile stresses and away from compressive stresses. This process is known as tensotaxis [2, 3, 10, 12, 20–22, 25, 26, 30].

One of the first experimental evidence that mechanical tension influences the behavior of cells can be found in [21]. To determine the effects of tension on epithelial motility

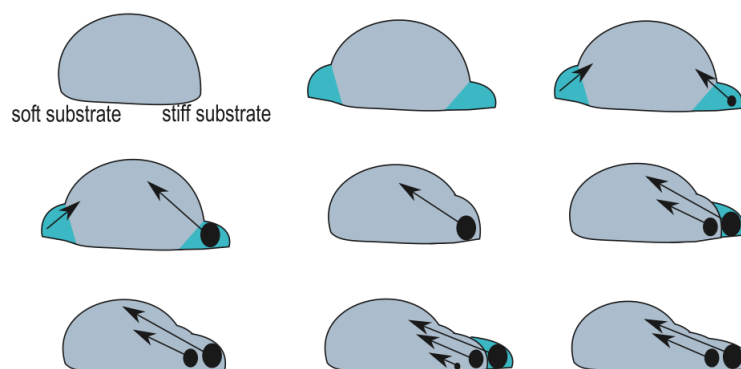


Figure 1.3: The cell forms protrusions (cyan) and it experiences a stiffer substrate on the right, so forces develop much faster on the right, allowing FAs to stabilize there. At the left, FAs fail to stabilize, allowing the cell to retract in order to propel itself forward and generate new FAs at the front. This continues and the cell moves to the right. Adapted from [8].

and cytoskeletal organization, small, motile clusters of epidermal cells were artificially extended with a micromanipulated needle; the authors observed that protrusive activity perpendicular to the axis of tension was dramatically suppressed and cytoskeletal microfilaments aligned themselves parallel to the tension.

Furthermore in [26] the authors investigated the effect of the tension arisen inside a mesodermal cell by pulling the cell body unidirectionally along the substratum. They proved that migratory cells tended to move in the direction away from the tractive force parallel to the substratum, suggesting that advancement of a leading lamella is accelerated when it is stretched along the direction of projection by a mechanical force of sufficient strength.

Further insights into this process were provided by Belussov et al. in [12]. They evaluated the behavior of the cells in a ventral ectodermic explant under stress and they observed that the cells moved to more strained regions of the substrate and showed that integrins were activated during migration. They also observed a stimulation of FAs when the substrate was strained.

Moreover, in a second series of experiments in the same article analyzed for durotaxis [2], Lo and co-workers externally pulled or pushed the substrate away or toward the cells center with a microneedle, and found a migration towards or away from the needle, respectively (see Fig. 1.4). They supposed that in the first case less motion is produced since cells experience a softening of the substrate, whereas in the second case the overall motion is increased since cells perceive the substrate as stiffer. They supposed then that durotaxis and tensotaxis are two processes linked each other. In this respect, it has been proposed that the process of mechanosensing could be mediated also by the energy of deformation involved in the cell–material interplay, in addition to stress and stiffness [3].

For what concerns the biological process involved in cell tenotaxis, the application of

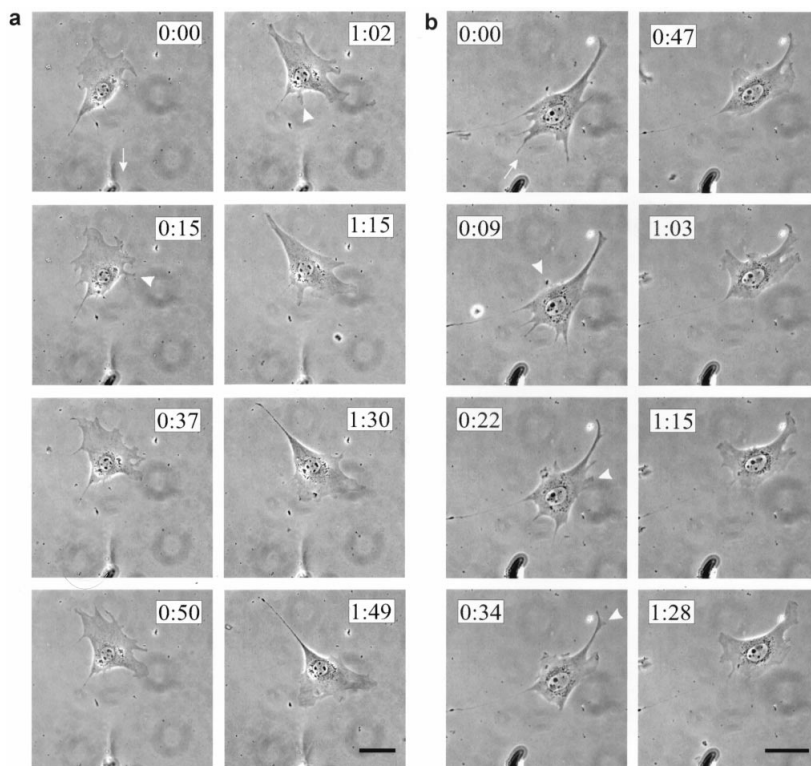


Figure 1.4: Figure showing experiments by Lo et al. [2] in which the substrate is stretched with a blunted microneedle. In panel (a) the needle was inserted near the rear part of a cell that was migrating away from it. The needle was then moved away from the cell, which changed its polarization and moved toward the needle. In panel (b) the needle was inserted near the front end of a cell that was migrating toward it. The needle was then moved toward the cell, which changed its polarization and moved away from the needle. The direction of movement of the microneedle is indicated by an arrow, and regions of lamellipodia development are indicated by arrowheads.

external stress/strain on the cell stimulates FAs formation and increases the tension that the submembrane plaque withstands. This tension can trigger molecular reorganization at the adhesion sites or alterations in the conformation of plaque proteins or integrins. That is the reason why the integrin-mediated submembrane plaque tension-dependent mechanism has been hypothesized as a possible mechanosensitive path [22].

1.2 Mathematical modeling background

Biology is one of the most fruitful field of study of applied mathematics: the formalization of biological processes through mathematical models is very helpful in order to better understand them and to be able to reproduce them for engineering and medical purposes.

Regarding the mechanism of chemotaxis, the mathematical models developed are innumerable and very diverse. From the Keller-Segel model [51], numerous continuous models, via partial differential equations systems for the evolving densities of cells and the concentrations of attractants/repellents, have been proposed in the last decades [40, 50]. In addition to continuous models, discrete models have also had significant development, both those describing the motion of a single cell and a collection of cells [49, 50]. For the purpose of this Thesis, among these single-cell discrete models, we cite the one presented by Colombi et al. in [1], that is an integro-differential non-local model in which a representative cell moves on a bidimensional substrate sensing signals from the surrounding environment in a non-local and non-isotropic way. The work of Colombi et al. [1] considers only chemical cues guiding cell motion. We will review in details the model in Section 2.1 explaining how this model could be adapt to describe the response of cells to mechanical stimuli.

Also for what concerns the area of cell motion driven by mechanical stimuli, theoretical and computational modeling approaches have provided insights, even if not comparable to those related to the process of chemotaxis. Moreo et al. [22] developed one of the first continuum mechanobiological model to study the adherent cell migration in a 2D environment. In this work, the cell-ECM interaction was characterized as an elastic spring system, representing the main components of the cell and matrix: microtubules of the cytoskeleton, actin bundles and the actomyosin machinery. The model predicted the phenomena of durotaxis and tensotaxis and suggested that their mechanisms involve the same cellular and matrix components. In [25] the authors generalized the same model to study the adherent cell migration in a porous medium, considering the influence of interstitial fluid on the behavior of cells and the extracellular matrix.

In the recent years several different models exploiting many mathematical and computational techniques have been proposed in order to study durotaxis and tensotaxis. In [8,9] the authors proposed a Cellular Potts Model to simulate single cell migration over flat substrates with variable stiffness, comparing the numerical results to specific experimental observations and showing a consistent agreement. In [18] the authors proposed a force-based, individual-based modeling framework that links single-cell migration with matrix fibers and cell-matrix interactions, highlighting the effect of the cell's environment on its migration. A model of a similar structure can be found in [33]: the authors developed a computational biomechanical model without any cell decision making to illuminate intrinsic mechanisms of durotactic behaviors of cells migrating on a two-dimensional substrate. The model consists of a simplified cell generating contractile forces and a deformable substrate coarse-grained into an irregular triangulated mesh. Using the model, they demonstrated that durotactic behaviors emerge from purely mechanical interactions between the cell and the underlying substrate and they investigated how durotactic migration is regulated by biophysical properties of the substrate, including elasticity, viscosity, and stiffness profile.

A hybrid discrete-continuum description of cells migrating on a substrate has been developed in [30]: an agent-based model for cell migration is developed, with moving probabilities that are influenced by deformations within the substrate and cells preferentially follow the direction of highest strain. A very different mathematical technique has been used in [10]: the authors used the level set method to study keratocyte evolution

Main author	Reference	Model	Processes	Dimensions
Merks	[8]	Hybrid CPM and FEM extended with ODE-based models of FA turnover	Durotaxis, evolution	FA 2D
Scianna	[9]	CPM	Durotaxis	2D
Rosakis	[10]	Level set method	Durotaxis, tenso-taxis, cell shape evolution	2D
Schluter	[18]	IBM	Durotaxis, cell-matrix interaction	2D
Bueno	[20]	Continuum model of fluid-structure interaction	Tensotaxis	2D, 3D
Moreo	[22]	Continuum	Durotaxis, tenso-taxis	2D
De Santis	[24]	Tensegrity	Durotaxis, tenso-taxis	1D, 3D
Rosalem	[25]	Continuum	Tensotaxis	2D
Chauviere	[30]	Hybrid discrete-continuum	Tensotaxis	2D
Malik	[31]	Stochastic, Fokker-Plank equation	Durotaxis	1D
Yu	[32]	Stochastic, Fokker-Plank equation	Durotaxis	2D
Hassan	[33]	Discrete	Durotaxis	2D

Table 1.1: Summary table with the models for cell migration due to mechanical stimuli reviewed in Section 1.2.

on flexible substrates, using mechanosensing concepts: cells apply contractile forces onto the elastic substrate, while cell shape evolution depends locally on the substrate stress generated by themselves or external mechanical stimuli acting on the substrate. They predict a number of distinct phenomena observed in experiments, among which there are durotaxis and tensotaxis.

Among other different kind of models in literature, we can find stochastic models that exploit Fokker-Planck equation [31,32], a tensegrity model to study the cell sensing of the elasticity of the substrate [24], a multiphysics phase-field model of fluid–solid interaction to understand the physics of tensotaxis [20].

Each model proposed in the literature focuses on different biological aspects of cellular motion and compares with experimental evidence, attempting to capture certain aspects. Each model must be considered taking into account its assumptions of validity, with the awareness that no model is perfect, but with the stimulus to try to approach models that are able to capture the most important aspects of the phenomenology under consideration while remaining as simple as possible. In Table 1.1 we gather the models for cell migration due to mechanical stimuli reviewed in this Section.

1.3 Aim and structure of the Thesis

The review done so far has focused on mathematical models that attempt to capture the mechanical aspects that stimulate cellular motion. On the other hand, with regard to the mechanism of chemotaxis, the work is certainly more advanced both from a biological and modeling perspective, as mentioned at the beginning of the previous Section. It seems therefore reasonable to adapt an established model of chemotaxis to account for the influence of mechanical stimuli on cell migration.

The aim of this Thesis is to present a new model for cell migration in response to mechanical cues, by combining the model proposed in [1] suitably modified with a model describing substrate mechanical behavior and its response in terms of deformations and stresses. The model is phenomenological and focuses more on the cellular scale than the subcellular mechanisms involved in the motion process. Despite its simplicity the model could be used to qualitative reproduce the experimental observations reported in [2].

The rest of the Thesis is organized as it follows. In Chapter 2 the mathematical model is presented. The equations of motion of the cell are 2D nonlocal integro-differential equations, with integral terms that are in charge of describing the nonlocal evaluation of the considered mechanical cue by the cell in its neighbourhood. While in the case of durotaxis the cell moves by changing its direction of polarization according to the different stiffness of the substrate, in the case of tensotaxis the substrate is appropriately deformed and the cell polarizes and migrates in response to proper scalar measures of the substrate strain or stress. In order to do so, the mass and momentum balance equations for the substrate are defined neglecting the mutual mechanical interaction between the cell and the substrate itself, that is modeled either as a linear elastic solid or as a hyperelastic Yeoh's solid.

In Chapter 3 the numerical implementation both of mechanical problem and of cell

migration model is addressed. The former is solved with the software *COMSOL Multiphysics*[®] and the quantities of interest are imported into a *MATLAB*[®] code that numerically implements the equations of motion. In particular the evaluation of the the integral terms calls for explicit numerical methods, as well as appropriate quadrature techniques to account for possible singularities of the integrand functions. In addition, it must be taken into account that the integrand functions may be defined only pointwise, and therefore their interpolation at quadrature nodes is necessary.

In Chapter 4 we set all the parameters involved and we validate the numerical implementation of the cell migration model, proposing the addition of a random term to the discretized equation of evolution of the cell center in order to obtain more realistic results. We then show the numerical simulations, which qualitatively agree with the experimental observations both in the case of durotaxis and tensotaxis.

In Chapter 5 we conclude the dissertation by summarizing the results we obtained, recalling the assumptions made and the limitations of our model. Finally we propose some possible modifications and expansions of the model for possible future works.

Chapter 2

The mathematical model

In this Chapter the mathematical model for 2D cell migration in response to mechanical stimuli is developed. As outlined in Section 1.3, our model combines the one proposed in [1] with a model describing substrate mechanical behavior and its response in terms of deformations and stresses. In Section 2.1 the original model is reviewed and properly adapted to our purposes and the equations of motion are derived in a general setting, so that several different mechanical stimuli can be taken into account.

While in the case of durotaxis it is sufficient to define the stiffness distribution over the substrate, if we want to account for the manipulation of the substrate its balance equations after the application of the load have to be solved in order to compute stresses, strains and energy. In Section 2.2 some basic notions of continuum mechanics are reviewed and the mass and momentum balance equations of the substrate (considered as an elastic media) are derived, following [7, 27].

We choose to decouple the mechanical problem of the substrate and the cell migration model, in the following sense: the load firstly acts on the substrate and deforms it, generating stresses and accumulating elastic energy, then the representative cell moves in response to these mechanical stimuli, without changing its shape or exerting a force on the substrate itself.

2.1 The model for cell migration

The position of the representative cell at time $t > 0$ is identified by the vector $\mathbf{x}_p(t) \in \mathbb{R}^2$, whereas its dimensions are taken into account by a sensing radius $R > 0$, representing the maximum extension of cell protrusions and identifying the sensing area $\mathcal{S}(\mathbf{x}_p)$ of the cell, that is the circle centered in \mathbf{x}_p and with radius R . Although we know that the cell sensing area is related to the cell shape and thus it is not necessarily circular, modeling its evolution along with its motion is not among the goals of our model, as it would complicate it unjustifiably. In fact, considering that we neglect the mechanical interaction between cell and substrate, assuming the shape of the cell to be constant and circular seems to be a fair compromise that does not considerably affect the trajectory of motion.

The cell velocity is defined as

$$\frac{d\mathbf{x}_p(t)}{dt} = v(t; m) \mathbf{w}(t; c), \quad (2.1)$$

in order to outline the cell actual scalar speed $v \in \mathbb{R}$ and its polarization $\mathbf{w} \in \mathbb{R}^2$, that identifies the direction of motion. While the former is related to cell motility, the latter is related to the process of organization of cell cytoskeletal filaments, which are able to align in response to external stimuli and to identify a preferred direction of locomotion [17]. Both quantities depends then on functions $c : \mathbb{R}_0^+ \times \mathbb{R}^2 \rightarrow \mathbb{R}$ and $m : \mathbb{R}_0^+ \times \mathbb{R}^2 \rightarrow [0,1]$, respectively. In [1], c is the concentration of a chemoattractants and m is the density fraction of extracellular proteins. Here we do not specify what these two functions physically represent, so that we will be able to simulate the different causes of motion with the same model, defining c and m as proper mechanical cues on the substrate in order to consider the case of durotaxis and tensotaxis. Following the original model in [1] we will properly normalize the function m we are going to choose, so that it can assume values in the interval $[0,1]$. In the following we will omit the dependence of \mathbf{w} and v on c and m respectively, taking

$$\mathbf{w}(t; c) = \mathbf{w}(t), \quad v(t; m) = v(t). \quad (2.2)$$

The polarization vector of the cell evolves according to

$$\frac{d\mathbf{w}(t)}{dt} = \frac{1}{\tau} \left(\frac{\mathbf{W}(t, \mathbf{x}_p(t), \mathbf{w}(t))}{\|\mathbf{W}(t, \mathbf{x}_p(t), \mathbf{w}(t))\| + \varepsilon} - \mathbf{w}(t) \right), \quad (2.3)$$

where $\mathbf{W} \in \mathbb{R}^2$ is the preferred axis of cell migration and it will be soon defined, the persistence time τ can be seen as the time needed by the cell to re-orient and $0 < \varepsilon \ll 1$ is a small parameter that ensures that $\|\mathbf{w}(t)\| \leq 1$ (being $\|\cdot\|$ the euclidean norm in \mathbb{R}^2) for any $t > 0$ if initially $\|\mathbf{w}(t=0)\| =: w_0 \in (0,1]$. In fact, the inner product of Eq. (2.3) by $\mathbf{w}(t)$ gives

$$\begin{aligned} \mathbf{w}(t) \cdot \frac{d\mathbf{w}(t)}{dt} &= \frac{1}{\tau} \left(\frac{\mathbf{W}(t, \mathbf{x}_p(t), \mathbf{w}(t)) \cdot \mathbf{w}(t)}{\|\mathbf{W}(t, \mathbf{x}_p(t), \mathbf{w}(t))\| + \varepsilon} - \|\mathbf{w}(t)\|^2 \right) \\ &\leq \frac{1}{\tau} \left(\frac{\|\mathbf{W}(t, \mathbf{x}_p(t), \mathbf{w}(t))\|}{\|\mathbf{W}(t, \mathbf{x}_p(t), \mathbf{w}(t))\| + \varepsilon} - \|\mathbf{w}(t)\| \right) \|\mathbf{w}(t)\|. \end{aligned} \quad (2.4)$$

Since

$$\mathbf{w}(t) \cdot \frac{d\mathbf{w}(t)}{dt} = \|\mathbf{w}(t)\| \frac{d\|\mathbf{w}(t)\|}{dt}, \quad (2.5)$$

it follows that

$$\frac{d\|\mathbf{w}(t)\|}{dt} \leq \frac{1}{\tau} \left(\frac{\|\mathbf{W}(t, \mathbf{x}_p(t), \mathbf{w}(t))\|}{\|\mathbf{W}(t, \mathbf{x}_p(t), \mathbf{w}(t))\| + \varepsilon} - \|\mathbf{w}(t)\| \right) \leq \frac{1}{\tau} (1 - \|\mathbf{w}(t)\|), \quad (2.6)$$

which in the end gives $\|\mathbf{w}(t)\| \leq 1 - (1 - w_0)e^{-t/\tau} \leq 1$ for any $t > 0$, as we intended to prove.

From Eq. (2.1) we may notice then that a partial polarization, that is $\|\mathbf{w}(t)\| < 1$, results in a slow down of cell displacement: if the cytoskeleton is not fully organized, the effective migratory capacity of the individual is in fact downregulated, since it is subjected to inputs coming from different directions that may inhibit each other.

In the following we will often omit time dependence of \mathbf{x}_p and \mathbf{w} to simplify the notation.

We define the cell preferred axis introduced in Eq. (2.3) as

$$\begin{aligned} \mathbf{W}(t, \mathbf{x}_p, \mathbf{w}) &= \frac{1}{A} \int_{\mathcal{S}(\mathbf{x}_p)} K \left(\|\mathbf{y} - \mathbf{x}_p\|, \frac{\mathbf{y} - \mathbf{x}_p}{\|\mathbf{y} - \mathbf{x}_p\|} \cdot \frac{\mathbf{w}}{\|\mathbf{w}\|} \right) c(t, \mathbf{y}) \frac{\mathbf{y} - \mathbf{x}_p}{\|\mathbf{y} - \mathbf{x}_p\|} d\mathbf{y} \\ &= \frac{1}{A} \int_0^R r \int_0^{2\pi} K \left(r, \mathbf{n}(\theta) \cdot \frac{\mathbf{w}}{\|\mathbf{w}\|} \right) c(t, \mathbf{x}_p + r\mathbf{n}(\theta)) \mathbf{n}(\theta) d\theta dr, \end{aligned} \quad (2.7)$$

where $\mathbf{y} = \mathbf{x}_p + r\mathbf{n}$, $r = \|\mathbf{y} - \mathbf{x}_p\|$ and $\mathbf{n} = (\mathbf{y} - \mathbf{x}_p) / \|\mathbf{y} - \mathbf{x}_p\| = (\cos \theta, \sin \theta)$. The scalar kernel $K : [0, R] \times [-1, 1] \rightarrow [0, 1]$ is a weight function that measures the capacity of the cell to sense the quantity given by c in a non-local and non-isotropic way, since its support actually identifies the individual sensing region. The constant A is nothing but a normalization constant, defined as

$$\begin{aligned} A &:= \int_{\mathcal{S}(\mathbf{x}_p)} K \left(\|\mathbf{y} - \mathbf{x}_p\|, \frac{\mathbf{y} - \mathbf{x}_p}{\|\mathbf{y} - \mathbf{x}_p\|} \cdot \frac{\mathbf{w}}{\|\mathbf{w}\|} \right) d\mathbf{y} \\ &= \int_0^R r \int_0^{2\pi} K \left(r, \mathbf{n}(\theta) \cdot \frac{\mathbf{w}}{\|\mathbf{w}\|} \right) d\theta dr, \end{aligned} \quad (2.8)$$

as usual in this kind of kernels of integral terms. The two arguments of K are the distance from the cell center of mass (*non-local sensing*) and the scalar product between the direction \mathbf{n} and the normalized polarization vector (*non-isotropic sensing*): assuming the independence of these two variations, we choose to model

$$K(r, u) = K_r(r) K_\theta(u), \quad (2.9)$$

with $K_r : [0, R] \rightarrow [0, 1]$ and $K_\theta : [-1, 1] \rightarrow [0, 1]$. In doing so, the cell preferred axis defined in Eq. (2.7) may be rewritten as

$$\mathbf{W}(t, \mathbf{x}_p, \mathbf{w}) = \frac{1}{A} \int_0^R r K_r(r) \int_0^{2\pi} K_\theta \left(\mathbf{n}(\theta) \cdot \frac{\mathbf{w}}{\|\mathbf{w}\|} \right) c(t, \mathbf{x}_p + r\mathbf{n}(\theta)) \mathbf{n}(\theta) d\theta dr, \quad (2.10)$$

where the weight function components, K_r and K_θ , and the distribution c should be suitably defined to result in a Riemann integrable integrand function. In Fig. 2.1, on the left, a representative case of the cell polarization process from [1] is shown.

For what concerns cell motility, we define the quantity

$$M(t, \mathbf{x}_p(t), \mathbf{w}(t)) = \frac{1}{R} \int_0^R m \left(\mathbf{x}_p(t) + r \frac{\mathbf{w}(t)}{\|\mathbf{w}(t)\|} \right) dr, \quad (2.11)$$

that is the mean of m perceived by the cell ahead along its polarization direction $\mathbf{w}(t)$ at time t (see Fig. 2.1, on the right), and we model $v(t)$ in Eq. (2.1) as

$$v(t) = v(t; m) = V_{max} f(M), \quad (2.12)$$

where $V_{max} > 0$ is the maximal cell speed and $f : [0,1] \rightarrow [0,1]$ measures the function m through the mean M non locally and it has to be modeled taking into account the cell mechanosensing system, as we will do in Chapter 4. For different choices of the quantity m we will use different functions f .

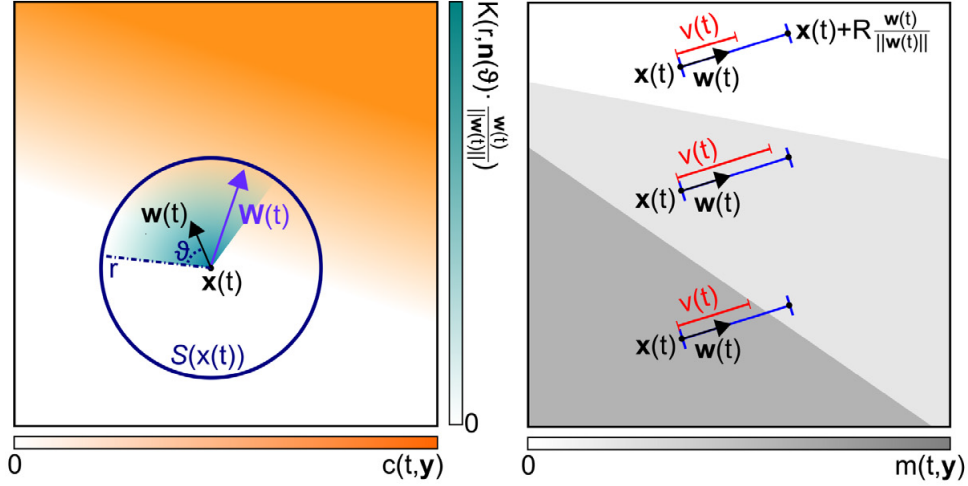


Figure 2.1: On the left, cell polarization process (i.e. the actual polarization \mathbf{w} and the preferred axis \mathbf{W}) is regulated only by the spatial distribution of the quantity c (see the orange shadow) within the cell sensing region $\mathcal{S}(\mathbf{x}_p(t))$ (see the blue circle), as perceived by the individual according to the weight function K (see the green shadow). On the right, cell intrinsic motility (i.e. the actual speed $v(t)$) depends only on the spatial distribution m non-locally perceived at its leading front. Both figure are reproduced from [1].

Summarizing, the whole model is a system of non-linear integro-differential equations made by Eqs. (2.1), (2.3), (2.10), (2.11), (2.12), an explicit expression of f in Eq. (2.12), and initial conditions $\mathbf{x}_p(0) = \mathbf{x}_{p0}$, $\mathbf{w}(0) = \mathbf{w}_0$. A proof for existence and uniqueness of the solution, as well as its continuous dependence on the initial condition, can be found in [1], in the case of a positive field c .

2.2 Substrate mechanics

After the introduction of the discrete model for cell migration, we need to model substrate mechanics to define its rigidity and to derive its equilibrium equations.

Because of their tunable mechanical properties, *polyacrylamide gels* (PAG) are frequently used for studying cell adhesion and migratory responses to extracellular substrate stiffness [2, 4, 5], mainly because PAG's elasticity can be easily and reproducibly tuned by adjusting the ratio of acrylamide and bis-acrylamide. In [4] it is outlined the fact that it is necessary to consider a non-linear elastic behaviour of the PAG in the context of cell traction force quantification and an explicit strain energy function is proposed. For the purposes of our model and according to the forces exerted in [2] to manipulate the

substrate, we will consider either a linear elastic behaviour or a hyperelastic behaviour as proposed in [4].

2.2.1 Finite deformations

Deformation and kinematics

In order to study the deformation and the motion of a continuum media, let \mathcal{B}_* be its *reference configuration* and let us denote the coordinates (X_L) of a particle in this configuration as *Lagrangian* (or *material*) *coordinates*. Then, we identify with \mathcal{B}_t the *current configuration* of the continuum at time t and we denote the coordinates (x_i) of a particle in this configuration as *Eulerian* (or *spatial*) *coordinates*. The motion is defined through a smooth map χ that assign to each material point \mathbf{X} at time t a point

$$\mathbf{x} = \chi(\mathbf{X}, t) \in \mathcal{B}_t, \quad \text{with} \quad (\mathbf{X}, t) \in \mathcal{B}_* \times [0, T]. \quad (2.13)$$

Equivalently, we can express Eq. (2.13) as

$$\mathbf{x}(\mathbf{X}, t) = \mathbf{X} + \mathbf{u}(\mathbf{X}, t), \quad (2.14)$$

where \mathbf{u} is the *displacement field* and its components read

$$\mathbf{u}(\mathbf{X}, t) = \begin{pmatrix} u(X, Y, Z, t) \\ v(X, Y, Z, t) \\ w(X, Y, Z, t) \end{pmatrix}, \quad (2.15)$$

since it is a function of the material point \mathbf{X} and of time. Differentiating Eq. (2.14) with respect to \mathbf{X} we get

$$\mathbb{F} = \mathbb{I} + \text{Grad } \mathbf{u}, \quad (2.16)$$

being $\text{Grad } \mathbf{u}$ the gradient of the displacement field

$$(\text{Grad } \mathbf{u})_{iL} = \frac{\partial u_i}{\partial X_L}, \quad (2.17)$$

\mathbb{I} the second order identity tensor, and \mathbb{F} the *deformation gradient tensor*, whose representative matrix in the Cartesian reference system is

$$\mathbb{F} = (F_{iL}) = \frac{\partial x_i}{\partial X_L}, \quad (2.18)$$

and it can be seen as a linear application that associates each infinitesimal vector $d\mathbf{X}$ in \mathbf{X} with the correspondent infinitesimal vector $d\mathbf{x}$ in \mathbf{x} , i.e.

$$d\mathbf{x} = \mathbb{F}d\mathbf{X}. \quad (2.19)$$

We furthermore require that $J := \det \mathbb{F} > 0$, to be consistent with the finite deformation hypothesis.

Given an infinitesimal surface element $d\Sigma_*$ and an infinitesimal volume element dV_* on \mathcal{B}_* , and the corresponding elements $d\Sigma$ and dV on \mathcal{B} , the following relations hold

$$d\Sigma = J\mathbb{F}^{-\top}d\Sigma_*, \quad dV = JdV_*. \quad (2.20)$$

Other tensors that will be useful for our purposes are the *right Cauchy-Green deformation tensor*

$$\mathbb{C} := \mathbb{F}^\top \mathbb{F}, \quad (2.21)$$

and the *Green-Lagrange finite strain tensor*

$$\mathbb{E} := \frac{1}{2} \left(\mathbb{F}^\top \mathbb{F} - \mathbb{I} \right) = \frac{1}{2} \left(\text{Grad } \mathbf{u} + (\text{Grad } \mathbf{u})^\top \right) + \frac{1}{2} (\text{Grad } \mathbf{u})^\top \text{Grad } \mathbf{u}, \quad (2.22)$$

that measures how much the deformed body differs from the undeformed one.

Focusing on kinematics, every quantity h associated to the motion can be expressed either in Lagrangian form if seen as a function of (\mathbf{X}, t) or in Eulerian form if seen as a function of (\mathbf{x}, t) , i. e.

$$h(\mathbf{x}, t) = h(\chi(\mathbf{X}, t), t) = \tilde{h}(\mathbf{X}, t). \quad (2.23)$$

The variation of \tilde{h} in time, that is $\frac{\partial \tilde{h}}{\partial t}(\mathbf{X}, t)$, will maintain the material point fixed, whereas $\frac{\partial h}{\partial t}(\mathbf{x}, t)$ will maintain the spatial coordinate fixed. To link these two variations we need to follow the point in its motion computing

$$\frac{dh}{dt}(\mathbf{x}(t), t) = \frac{\partial h}{\partial t}(\mathbf{x}(t), t) + \mathbf{v}(\mathbf{x}(t), t) \cdot \nabla h(\mathbf{x}(t), t), \quad (2.24)$$

where

$$\mathbf{v} := \frac{\partial \chi}{\partial t}(\mathbf{X}, t) \quad (2.25)$$

is the *velocity field*. In this way we may define the *acceleration* (in Lagrangian form) of the particle \mathbf{X} at the time instant t as

$$\mathbf{a}(\mathbf{X}, t) = \frac{\partial^2 \chi}{\partial t^2}(\mathbf{X}, t), \quad (2.26)$$

or in Eulerian form as

$$\mathbf{a}(\mathbf{x}, t) = \frac{\partial \mathbf{v}}{\partial t}(\mathbf{x}(t), t) + \mathbf{v}(\mathbf{x}(t), t) \cdot \nabla \mathbf{v}(\mathbf{x}(t), t). \quad (2.27)$$

Balance laws

In a continuum body we suppose the mass to be distributed all over the region \mathcal{B}_t . Then, we suppose the existence of a *density mass function* $\rho(\mathbf{x}, t)$ and the *mass balance law* can be written either in integral form as

$$\frac{d}{dt} \int_{\mathcal{V}_t} \rho(\mathbf{x}, t) dV = 0, \quad \forall \mathcal{V}_t \subseteq \mathcal{B}_t, \quad (2.28)$$

or in local form in Eulerian coordinates as

$$\frac{\partial \rho}{\partial t} + \nabla \cdot (\rho \mathbf{v}) = 0, \quad \text{in } \mathcal{B}_t, \quad (2.29)$$

where $\nabla \cdot$ denotes the divergence operator with respect to the Eulerian coordinates. Equivalently, the mass balance law can be expressed in Lagrangian form equating

$$\rho_*(\mathbf{X}) dV_* = \rho(\mathbf{x}, t) dV, \quad (2.30)$$

and exploiting Eq. (2.20) we get

$$\rho_* = \rho J, \quad (2.31)$$

being $\rho_*(\mathbf{X})$ the density mass function over the reference configuration \mathcal{B}_* .

Let us now consider the continuum subject to a body load per unit volume \mathbf{b} and a surface load per unit surface \mathbf{t} . The *first cardinal equation*, or balance of momentum, can be expressed in integral form as

$$\frac{d}{dt} \int_{\mathcal{V}_t} \rho \mathbf{v} dV = \int_{\mathcal{V}_t} \mathbf{b} dV + \int_{\partial \mathcal{V}_t} \mathbf{t} d\Sigma \quad (2.32)$$

where $\mathcal{V}_t \subseteq \mathcal{B}_t$ is a subdomain of the body and $\partial \mathcal{V}_t$ is its closed and smooth surface.

We follow the *Cauchy hypothesis of simple continuum*, that ensures the dependence

$$\mathbf{t} = \mathbf{t}(\mathbf{x}, t, \mathbf{n}), \quad \mathbf{x} \in \partial \mathcal{V}_t, \quad (2.33)$$

being \mathbf{n} the outward normal vector to the surface. Under this hypothesis the well known *Cauchy theorem* guarantees the existence and uniqueness of the second order *stress tensor* \mathbb{T} , such that the surface load may be written as

$$\mathbf{t} = \mathbb{T} \mathbf{n}. \quad (2.34)$$

Thanks to the *second cardinal equation*, or balance of angular momentum, that ensures that \mathbb{T} is a symmetric tensor, and to Gauss divergence theorem, Eq. (2.32) may be easily rewritten in local Eulerian form as

$$\rho \mathbf{a} = \nabla \cdot \mathbb{T} + \mathbf{b}, \quad \text{in } \mathcal{B}_t. \quad (2.35)$$

In order to write Eq. (2.35) in Lagrangian coordinates, we exploit the relations (2.20) and rewrite the balance of momentum as

$$\frac{d}{dt} \int_{\mathcal{V}_*} \rho_* \mathbf{v} J dV_* = \int_{\mathcal{V}_*} \mathbf{b} J dV_* + \int_{\partial \mathcal{V}_*} \mathbb{P} \mathbf{N} d\Sigma_*, \quad (2.36)$$

where

$$\mathbb{P} = J \mathbb{T} \mathbb{F}^{-\top} \quad (2.37)$$

is the *first Piola-Kirchhoff stress tensor*. Eq. (2.36) can be written in local form as

$$\rho_* \mathbf{a} = \mathbf{b} J + \text{Div } \mathbb{P}, \quad (2.38)$$

being $\text{Div}(\cdot)$ the divergence operator with respect to the Lagrangian coordinates, whereas the balance of angular momentum reads

$$\mathbb{P}\mathbb{F}^\top = \mathbb{F}\mathbb{P}^\top, \quad (2.39)$$

since \mathbb{P} is a two-point tensor and it cannot be symmetric. Indeed, it relates forces in the current configuration with areas in the reference configuration, whereas the Cauchy stress tensor \mathbb{T} relates forces in the current configuration with areas in the current configuration itself.

Principal stresses and strains

At every point in a stressed body there are at least three planes, called *principal planes*, with normal vectors \mathbf{n} , called *principal directions*, where the corresponding stress vector is perpendicular to the plane, i.e. parallel to the normal vector \mathbf{n} , and where there are no normal shear stresses. The three stresses normal to these principal planes are called *principal stresses*. Then, finding these principal directions and stresses is equivalent to solve the eigenvalues equation

$$\mathbb{T}\mathbf{n} = \sigma_n\mathbf{n}, \quad (2.40)$$

with $\mathbf{n} \neq \mathbf{0}$. In a Cartesian coordinate system the symmetric tensor \mathbb{T} has the generical matricial representation

$$\mathbb{T} = \begin{pmatrix} \sigma_{xx} & \sigma_{xy} & \sigma_{xz} \\ \sigma_{xy} & \sigma_{yy} & \sigma_{yz} \\ \sigma_{xz} & \sigma_{yz} & \sigma_{zz} \end{pmatrix}, \quad (2.41)$$

and solving Eq. (2.40) requiring

$$\det(\mathbb{T} - \sigma_n\mathbb{I}) = 0 \quad (2.42)$$

(being $\det(\cdot)$ the *determinant operator* and \mathbb{I} the second order identity tensor), leads to the cubic algebraic equation

$$\sigma_n^3 - I_1\sigma_n^2 + I_2\sigma_n - I_3 = 0, \quad (2.43)$$

where

$$I_1 = \sigma_{xx} + \sigma_{yy} + \sigma_{zz} = \text{tr } \mathbb{T}, \quad (2.44)$$

$$I_2 = \sigma_{xx}\sigma_{yy} + \sigma_{xx}\sigma_{zz} + \sigma_{yy}\sigma_{zz} - \sigma_{xy}^2 - \sigma_{xz}^2 - \sigma_{yz}^2 = \frac{1}{2} \left((\text{tr } \mathbb{T})^2 - \text{tr}(\mathbb{T}^2) \right), \quad (2.45)$$

$$I_3 = \sigma_{xx}\sigma_{yy}\sigma_{zz} + 2\sigma_{xy}\sigma_{xz}\sigma_{yz} - \sigma_{xy}^2\sigma_{zz} - \sigma_{xz}^2\sigma_{yy} - \sigma_{yz}^2\sigma_{xx} = \det \mathbb{T} \quad (2.46)$$

are the first, second, and third *stress invariants*, respectively (being $\text{tr}(\cdot)$ the *trace operator*), and they always have the same value regardless of the coordinate system's orientation. In particular, the first stress invariant is a measure of the mean stress applied to the body. Due to the stress tensor symmetry, Eq. (2.43) leads to three real solutions $\sigma_1, \sigma_2, \sigma_3$, that can be inserted in Eq. (2.40) in order to compute the three principal directions $\mathbf{n}_1, \mathbf{n}_2, \mathbf{n}_3$. A coordinate system with axes oriented to the principal directions implies

that the normal stresses are the principal stresses and the stress tensor is represented by a diagonal matrix

$$\mathbb{T} = \begin{pmatrix} \sigma_1 & 0 & 0 \\ 0 & \sigma_2 & 0 \\ 0 & 0 & \sigma_3 \end{pmatrix}, \quad (2.47)$$

and also the stress invariants may be written in terms of the principal stresses as

$$I_1 = \sigma_1 + \sigma_2 + \sigma_3, \quad (2.48)$$

$$I_2 = \sigma_1\sigma_2 + \sigma_1\sigma_3 + \sigma_2\sigma_3, \quad (2.49)$$

$$I_3 = \sigma_1\sigma_2\sigma_3. \quad (2.50)$$

We can proceed in an analogous way with the symmetric right Cauchy-Green deformation tensor $\mathbb{C} = \mathbb{F}^\top \mathbb{F}$ denoting its eigenvalues with $\lambda_1, \lambda_2, \lambda_3$ and its invariants with

$$J_1 = \lambda_1 + \lambda_2 + \lambda_3, \quad (2.51)$$

$$J_2 = \lambda_1\lambda_2 + \lambda_1\lambda_3 + \lambda_2\lambda_3, \quad (2.52)$$

$$J_3 = \lambda_1\lambda_2\lambda_3. \quad (2.53)$$

However, it is important to highlight that the principal directions of the stress are defined over the deformed configuration, whereas the principal directions of the strain are defined over the undeformed one.

Hyperelastic solid

Solving the continuum balance laws means computing the density ρ , the displacement field \mathbf{u} (or equivalently the map χ) and the stress tensor \mathbb{T} (or equivalently \mathbb{P}). In order to do so, we need to add a relation between the deformations and the stresses, that is we need to specify the *constitutive relation* of the material.

As said at the beginning of the Chapter, we model the substrate as a *hyperelastic solid*. Among all the possible choice of stress-strain relations, we define a solid to be hyperelastic if there exists a *strain energy density function* $W(\mathbb{E})$ such that

$$\mathbb{P}(\mathbb{E}) = \mathbb{F} \frac{\partial W}{\partial \mathbb{E}}. \quad (2.54)$$

This choice is useful because we will solve the balance equations (2.38) in Lagrangian form, as usual in the context of solid mechanics due to the presence of a well defined reference configuration.

It is then sufficient to define the function $W(\mathbb{E})$ to close properly the system of equations. We assume the *isotropy* of the material, that guarantees that there are no preferred directions for stresses: an applied force will give the same displacements no matter the direction in which the force is applied. Thanks to this assumption and to the *objectivity principle* [27] it can be proved that the energy W depends only on the invariants of \mathbb{E} , or equivalently on the invariants of \mathbb{C} , and on $J = \det \mathbb{F}$, that is

$$W(\mathbb{E}) = \tilde{W}(J_1, J_2, J_3, J). \quad (2.55)$$

Following [4], we choose to use Yeoh’s energy density function

$$\tilde{W}(J_1, J_2, J_3, J) = \hat{W}(J_1, J) = \sum_{n=1}^3 c_n (J^{-2/3} J_1 - 3)^n + c_4 (J - 1)^2, \quad (2.56)$$

where the material coefficients c_1, c_2, c_3, c_4 have to be defined.

2.2.2 Small deformations

To account also for a linearly elastic behaviour of the substrate, we consider here the case of *small deformations*.

A deformation between two different configurations of the continuum body is *infinitesimal* if $\|\text{Grad } \mathbf{u}\| \ll 1$. This means that we can approximate at the first order Eq. (2.16) to

$$\mathbb{F} \approx \mathbb{I} \quad (2.57)$$

and we can therefore use equivalently either Lagrangian or Eulerian coordinates. Furthermore the stress tensors \mathbb{T} and \mathbb{P} approximately coincide. In doing so, Eq. (2.54) for the elasticity assumption can be written as

$$\mathbb{T}(\boldsymbol{\varepsilon}) = \frac{\partial W}{\partial \boldsymbol{\varepsilon}}, \quad (2.58)$$

being $\boldsymbol{\varepsilon}$ the *infinitesimal strain tensor*, nothing but the linearization of \mathbb{E} :

$$\mathbb{E} \approx \frac{1}{2} \left(\text{Grad } \mathbf{u} + (\text{Grad } \mathbf{u})^\top \right) =: \boldsymbol{\varepsilon}. \quad (2.59)$$

Through the small deformations approximation it can be proved that the energy is a quadratic function of the strain, in formulas

$$W(\boldsymbol{\varepsilon}) = \frac{1}{2} \boldsymbol{\varepsilon} \cdot \mathcal{C} \boldsymbol{\varepsilon}, \quad (2.60)$$

where the symbol “ \cdot ” denotes the tensor inner product and \mathcal{C} is a fourth-order tensor called *elasticity tensor*. It has $3^4 = 81$ components, but through considerations on its symmetries it can be shown that there are 21 independent components, in a general setting, depending on the solid mechanical properties. The stress tensor can now derived as

$$\mathbb{T}(\boldsymbol{\varepsilon}) = \mathcal{C} \boldsymbol{\varepsilon}, \quad (2.61)$$

that is nothing but a generalization of the well known *Hooke’s law* for linear elasticity.

Assuming isotropy it can be shown that the independent components of the elasticity tensor \mathcal{C} reduce to two. Among all possibilities, we choose to use the *Young modulus* E and the *Poisson coefficient* ν , so that the stress tensor reads

$$\mathbb{T}(\boldsymbol{\varepsilon}) = \frac{E}{1 + \nu} \boldsymbol{\varepsilon} + \frac{\nu E}{(1 + \nu)(1 - 2\nu)} \text{tr}(\boldsymbol{\varepsilon}) \mathbb{I}. \quad (2.62)$$

The modulus E and the coefficient ν are in general function of the material point of the body; however, if the solid is *homogeneous* they are independent of position and reduce to simple constants, depending on the material. In particular, E is a mechanical property that measures the tensile or compressive stiffness of a solid material when the force is applied lengthwise.

Inserting Eq. (2.62) in the balance of momentum we derive an explicit equation for the displacement field

$$\rho \frac{\partial^2 \mathbf{u}}{\partial t^2} = \frac{E}{2(1+\nu)} \left(\nabla^2 \mathbf{u} + \frac{1}{1-2\nu} \nabla (\nabla \cdot \mathbf{u}) \right) + \mathbf{b}, \quad (2.63)$$

known as *Navier-Cauchy equation*.

2.2.3 Plane stress approximation

Many problems in elasticity can be simplified as two-dimensional problems described by plane theory of elasticity. In general there are two types of problems we may encounter in plane analysis: *plane stress* and *plane strain*. The first problem arises in analysis of thin plates loaded in the plane of the plate, while the second is used for elongated bodies of constant cross section subject to uniform loading. The mechanical problem we will deal with is part of the former case, so we now develop the approximated equations for the plane stress conditions.

Plane stress distributions build on the assumption that the normal stress and shear stresses directed perpendicular to the XY plane are negligible. Referring on a Cartesian coordinate system as in Eq. (2.41) we have

$$\sigma_{xz} = \sigma_{yz} = \sigma_{zz} = 0. \quad (2.64)$$

It is also assumed that all the functions do not vary through the thickness of the substrate, so that they are spatial functions of X and Y only:

$$u = u(X, Y), \quad v = v(X, Y), \quad (2.65)$$

$$\varepsilon_{xx} = \varepsilon_{xx}(X, Y), \quad \varepsilon_{yy} = \varepsilon_{yy}(X, Y), \quad \varepsilon_{xy} = \varepsilon_{xy}(X, Y), \quad (2.66)$$

$$\sigma_{xx} = \sigma_{xx}(X, Y), \quad \sigma_{yy} = \sigma_{yy}(X, Y), \quad \sigma_{xy} = \sigma_{xy}(X, Y). \quad (2.67)$$

These assumptions are approximations, but they are still sufficiently accurate for practical applications if the substrate is thin and if the interaction with the cell is neglected, as in the case we are dealing with. Furthermore, we highlight that the displacement w and the strains $\varepsilon_{xz}, \varepsilon_{yz}, \varepsilon_{zz}$ along the Z axis are not necessary null, but within the context of plane stress approximation they become secondary variables and we will not compute them.

Taking these considerations into account, with straightforward computations we can derive the balance equation for the plane stress approximation in a similar way as done for Eq. (2.63) and we get:

$$\rho \frac{\partial^2 \mathbf{u}}{\partial t^2} = \frac{E}{2(1+\nu)} \left(\nabla^2 \mathbf{u} + \frac{1+\nu}{1-\nu} \nabla (\nabla \cdot \mathbf{u}) \right) + \mathbf{b}, \quad (2.68)$$

in which we have renamed $\mathbf{u} = (u, v)^\top$ for simplicity. Unlike Eq. (2.63), Eq. (2.68) has to be solved in a two-dimensional domain and the boundary conditions must be set in the same domain too, simplifying the problem. For what concerns the body force \mathbf{b} , in order to deal with the 2D approximation we set

$$\mathbf{b} = \frac{\mathbf{b}_s}{h}, \quad (2.69)$$

where h is the substrate thickness and \mathbf{b}_s is the force per unit surface applied on the bidimensional domain.

Within the context of finite deformation, the assumptions made on the tensors \mathbb{T} and $\boldsymbol{\varepsilon}$ can be generalized for the tensors \mathbb{P} and \mathbb{E} . We do not derive a simplified equations as Eq. (2.68), but the advantages of dealing with a bidimensional domain are the same.

Chapter 3

Numerical implementation

The model proposed in the previous Chapter cannot be solved analytically, so a numerical implementation is needed. Specifically, we will deal with the mechanical problem of the substrate in the case of tensotaxis in Section 3.1, in order to compute stresses and strains and to be able to choose the proper scalar measures c and m for the cell migration model. The numerical implementation of the latter is analyzed in Section 3.2 for generic stimuli, taking account of several different numerical issues.

3.1 Mechanical manipulation of the substrate

We model the substrate on which the cell migrates as a thin parallelepiped of thickness h and with square faces of length L . Since the mechanical load we will apply is a microneedle inserted in the substrate and moved along its plane as in [2], we are in a plane stress approximation regime as outlined in Subsection 2.2.3 and the problem can be solved in the bidimensional squared domain $\Omega = [0, L] \times [0, L]$. Assuming a static load condition, if we consider a non-linear elastic behaviour of the substrate the system of mechanical equations in Lagrangian form reads

$$\frac{\mathbf{b}_s}{h} J + \text{Div } \mathbb{P} = \mathbf{0}, \quad (3.1)$$

$$\mathbb{P}(\mathbb{E}) = \mathbb{F} \frac{\partial W}{\partial \mathbb{E}}, \quad (3.2)$$

$$W(\mathbb{E}) = \hat{W}(J_1, J) = \sum_{n=1}^3 c_n (J^{-2/3} J_1 - 3)^n + c_4 (J - 1)^2, \quad (3.3)$$

$$\mathbb{E} = \frac{1}{2} (\mathbb{F}^\top \mathbb{F} - \mathbb{I}), \quad \mathbb{F} = \mathbb{I} + \text{Grad } \mathbf{u}, \quad (3.4)$$

where $J = \det \mathbb{F}$ and J_1 is the trace of $\mathbb{C} = \mathbb{F}^\top \mathbb{F}$. The system reduces to the equation

$$\frac{E}{2(1+\nu)} \left(\nabla^2 \mathbf{u} + \frac{1+\nu}{1-\nu} \nabla (\nabla \cdot \mathbf{u}) \right) + \frac{\mathbf{b}_s}{h} = \mathbf{0}, \quad (3.5)$$

if the substrate is modeled as linearly elastic. In both cases, the unknown is the displacement field $\mathbf{u} = (u, v)^\top$, that must satisfy the boundary condition

$$\mathbf{u} = \mathbf{0} \quad \text{on} \quad \partial\Omega, \quad (3.6)$$

since it is experimentally detected that the edges of the substrate are fixed [2].

The manipulation with the microneedle is modeled in the load per unite surface \mathbf{b}_s . The needle pushes or pulls the substrate along a direction identified by an angle $\beta \in [0, 2\pi)$, localized in a circle $\mathcal{D} \subset \Omega$ sufficiently far from the boundary, and with intensity f_b . Taking all these considerations in account, the load is

$$\mathbf{b}_s = f_b \begin{pmatrix} \cos \beta \\ \sin \beta \end{pmatrix} \mathbb{1}_{\mathcal{D}}, \quad (3.7)$$

being $\mathbb{1}_{\mathcal{D}}$ the characteristic function of the set \mathcal{D} . A representative case of the domain and an applied load is shown in Fig. 3.1.

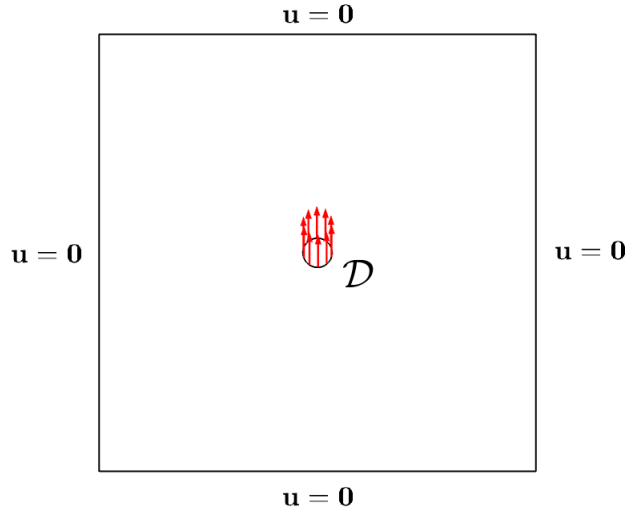


Figure 3.1: The squared domain $\Omega = [0, L] \times [0, L]$ with a small circle \mathcal{D} in the center that models the manipulation with the needle ($\beta = \pi/2$ in Eq. 3.7) and with the boundary condition $\mathbf{u} = \mathbf{0}$ on $\partial\Omega$.

The problem is then solved with the Finite Element Method (FEM), using the *Structural Mechanics Module* of the software *COMSOL Multiphysics*[®]. The *Physics-controlled* mesh is automatically generated, with *Finer* element size [34]. A representative case of a meshed domain is shown in panel (a) of Fig. 3.2.

The solution or any quantity of interest is then exported in a $\Lambda \times \Lambda$ tensor grid with the length step $\Delta y = L/\Lambda$ in both directions, as shown in panel (b) of Fig. 3.2, so that it can be used as external signal for the cell migration model. In this way an interpolation automatically performed by the software is implied, from the vertices of the mesh to the regular tensor grid.

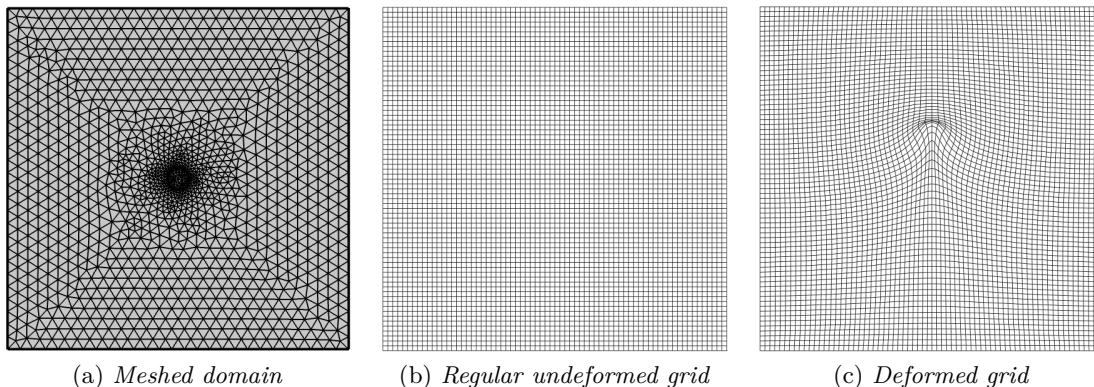


Figure 3.2: Panel (a) shows an example of a triangular mesh for the domain Ω automatically generated by the software *COMSOL Multiphysics*[®] to solve the mechanical problem. Panel (b) shows an example of a $\Lambda \times \Lambda$ tensor grid with $\Lambda = 70$. Panel (c) shows the same grid of panel (b) when deformed as defined in Eq. (3.13).

3.2 Time-integration for the cell migration model

The numerical implementation of the model for cell migration derived in Section 2.1 is here tackled, referring to [6] for the theoretical numerical methods involved. We recall here the model is

$$\frac{d\mathbf{x}_p(t)}{dt} = v(t) \mathbf{w}(t), \quad (3.8)$$

$$\frac{d\mathbf{w}(t)}{dt} = \frac{1}{\tau} \left(\frac{\mathbf{W}(t, \mathbf{x}_p(t), \mathbf{w}(t))}{\|\mathbf{W}(t, \mathbf{x}_p(t), \mathbf{w}(t))\| + \varepsilon} - \mathbf{w}(t) \right), \quad (3.9)$$

$$\mathbf{W}(t, \mathbf{x}_p, \mathbf{w}) = \frac{1}{A} \int_0^R r K_r(r) \int_0^{2\pi} K_\theta \left(\mathbf{n}(\theta) \cdot \frac{\mathbf{w}}{\|\mathbf{w}\|} \right) c(t, \mathbf{x}_p + r\mathbf{n}(\theta)) \mathbf{n}(\theta) d\theta dr, \quad (3.10)$$

$$M(t, \mathbf{x}_p(t), \mathbf{w}(t)) = \frac{1}{R} \int_0^R m \left(\mathbf{x}_p(t) + r \frac{\mathbf{w}(t)}{\|\mathbf{w}(t)\|} \right) dr, \quad (3.11)$$

$$v(t) = V_{max} f(M), \quad (3.12)$$

with explicit expressions of K_r , K_θ and f that will be given in Chapter 4.

First of all, the numerical approximation of the integrals \mathbf{W} and M in Eqs. (3.10) and (3.11) respectively requires suitable quadrature formulas, able to handle possible non-regularities of the integrand functions. In order to simplify the problem, we require the kernels K_r and K_θ to be continuous, but the functions c and m can be discontinuous, even if piecewise regular, e.g. a piecewise constant substrate stiffness. A tailored application of the Gauss-Legendre quadrature formula is proposed and adapted from [1], consisting in applying the formula in each subregion of the integration domains ($\mathcal{S}(\mathbf{x}_p)$ and $[0, R]$, respectively) where the integrand functions are actually smooth. Having in mind that the accuracy of a Gaussian quadrature rule depends on the smoothness of the integrand

(i.e., the higher the regularity of the integrand function is, the faster the convergence of the quadrature formula is), we expect that such an *ad hoc* approach turns out to be more accurate and efficient than a standard application of the quadrature formula to the entire domain of integration.

Furthermore, the time integration of the proposed model involves at each time step the evaluation of the integral terms \mathbf{W} and M : it requires then an explicit ODE solver, e.g. the first and second-order explicit Runge–Kutta methods, known as Euler and Heun method respectively.

Besides, the functions c and m may not be analytically defined, e.g. experimental measured or imported from the software in which the mechanical problem for the substrate is solved. If this is the case, they are defined only over a finite amount of points, that may not coincide in general with the quadrature nodes needed to evaluate the integral terms (see Fig. 3.3): it is then necessary to use a suitable interpolation method to approximate the missing data, preserving the accuracy and efficiency of the overall numerical scheme.

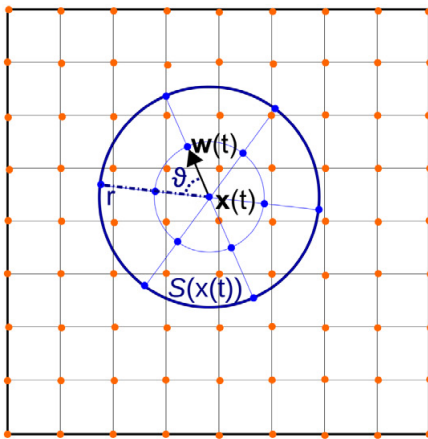


Figure 3.3: Representative case where the distribution c is defined only over a finite amount of points (i.e. the orange dots) which do not coincide with the quadrature nodes (i.e. the blue dots) required to evaluate \mathbf{W} (from [1]).

In particular, if the signals come from the mechanical problem, they are defined over a tensor grid as in Panel (b) of Fig. 3.2 in Lagrangian coordinates. However, the cell migrates over the substrate already deformed sensing those mechanical signals, so it migrates over the *current configuration* of the substrate. Then, the quantities of interest have to be considered as functions of the Eulerian coordinates as in Eq. (2.23).

To tackle this issue it is sufficient to properly deform the grid taking into account the computed deformation field \mathbf{u} . Denoting by $\mathbf{X}_{ij} \in \Omega$ the points of the regular grid, with $i, j = 1, \dots, \Lambda$, the deformed one is identified by the points

$$\mathbf{x}_{ij} = \mathbf{X}_{ij} + \mathbf{u}(\mathbf{X}_{ij}), \quad (3.13)$$

such that

$$c(t, \mathbf{X}_{ij}) = c(t, \mathbf{x}_{ij}), \quad m(t, \mathbf{X}_{ij}) = m(t, \mathbf{x}_{ij}). \quad (3.14)$$

A representative example of a deformed grid is shown in panel (c) of Fig. 3.2, and an example of a field in both Lagrangian and Eulerian form (or plotted on the undeformed grid or on the deformed one, equivalently) is shown in Fig. 3.4.

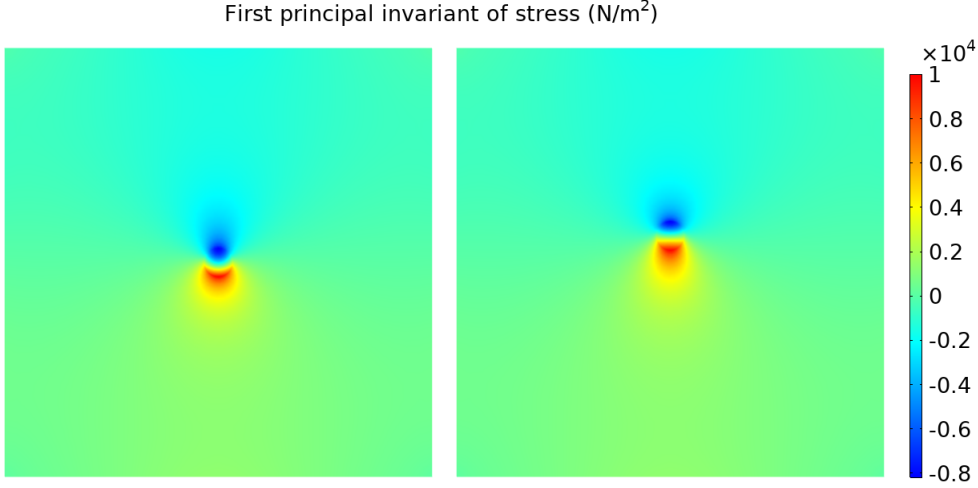


Figure 3.4: On the left, a stress field in Lagrangian form (or plotted on the undeformed tensor grid as in panel (b) of Fig. 3.2, equivalently). On the right, the same stress field in Eulerian form (or plotted on the correspondent deformed grid as in panel (c) of Fig. 3.2, equivalently).

3.2.1 Explicit Runge-Kutta methods

In order to apply the proper method, we first rewrite Eqs. (3.8) and (3.9) in the following canonical form

$$\begin{cases} \frac{d\mathbf{z}(t)}{dt} = \mathbf{F}(t, \mathbf{z}(t)), & t \in (0, T], \\ \mathbf{z}(0) = \mathbf{z}_0, \end{cases} \quad (3.15)$$

defining

$$\mathbf{z}(t) := \begin{pmatrix} \mathbf{x}_p(t) \\ \mathbf{w}(t) \end{pmatrix}, \quad \mathbf{F}(t, \mathbf{z}(t)) := \begin{pmatrix} \mathbf{g}_x(t, \mathbf{x}_p(t), \mathbf{w}(t)) \\ \mathbf{g}_w(t, \mathbf{x}_p(t), \mathbf{w}(t)) \end{pmatrix}, \quad (3.16)$$

where \mathbf{g}_x and \mathbf{g}_w denote the right hand sides of Eqs. (3.8) and (3.9), respectively. We then introduce a uniform partitioning of the time interval $(0, T]$ into N subintervals of length $\Delta t = T/N$ and we denote by $t_n = n\Delta t$, with $n = 0, \dots, N$ the $N + 1$ time instants associated to the discretization. As usual in numerical integration of ODE, we will compute the solution $\mathbf{z}(t)$ only over the time instants t_n , denoting by \mathbf{z}_n the approximated value of $\mathbf{z}(t_n)$. Starting from the initial value $\mathbf{z}_0 = (\mathbf{x}_{p0}, \mathbf{w}_0)^\top$ we may apply either the Euler method computing

$$\mathbf{z}_{n+1} = \mathbf{z}_n + \Delta t \mathbf{F}(t_n, \mathbf{z}_n), \quad (3.17)$$

or the Heun method computing

$$\mathbf{z}_{n+1} = \mathbf{z}_n + \frac{\Delta t}{2} \left[\mathbf{F}(t_n, \mathbf{z}_n) + \mathbf{F}(t_{n+1}, \mathbf{z}_n + \Delta t \mathbf{F}(t_n, \mathbf{z}_n)) \right], \quad (3.18)$$

for $n = 0, \dots, N - 1$.

If a mechanical manipulation of the substrate occurs, it is necessary to clarify that the initial position $\mathbf{x}_{p0} \in \Omega$ of the cell is defined before the deformation. Then, similarly as done in Eq. (3.13), we must replace the initial condition \mathbf{x}_{p0} with

$$\mathbf{x}_{p0} + \mathbf{u}(\mathbf{x}_{p0}), \quad (3.19)$$

since the cell is anchored to the substrate during the deformation.

3.2.2 Tailored Gauss-Legendre quadrature formula

As highlighted before, we note that the the evaluation of the functions \mathbf{g}_x and \mathbf{g}_w is needed at each time step, and this requires the computation of the integrals \mathbf{W} and M defined in Eqs. (3.10) and (3.11), respectively (see Fig. 3.3). For what concerns the double integral $\mathbf{W}_n := \mathbf{W}(t_n, \mathbf{x}_{pn}, \mathbf{w}_n)$, we apply a $\nu \times \bar{\nu}$ Gauss-Legendre quadrature formula, that is

$$\begin{aligned} \mathbf{W}_n &= \frac{1}{A} \int_0^R r K_r(r) \int_0^{2\pi} K_\theta \left(\mathbf{n}(\theta) \cdot \frac{\mathbf{w}_n}{\|\mathbf{w}_n\|} \right) c(t_n, \mathbf{x}_{pn} + r \mathbf{n}(\theta)) \mathbf{n}(\theta) d\theta dr \\ &\approx \frac{1}{A} \sum_{p=1}^{\nu} w_p r_p K_r(r_p) \sum_{q=1}^{\bar{\nu}} \bar{w}_q K_\theta \left(\mathbf{n}(\theta_q) \cdot \frac{\mathbf{w}_n}{\|\mathbf{w}_n\|} \right) c(t_n, \mathbf{x}_{pn} + r_p \mathbf{n}(\theta_q)) \mathbf{n}(\theta_q), \end{aligned} \quad (3.20)$$

where w_p and r_p , \bar{w}_q and θ_q ($p = 1, \dots, \nu$, $q = 1, \dots, \bar{\nu}$) are the weights and the nodes of the ν -point and $\bar{\nu}$ -point Gauss-Legendre formula in $[0, R]$ and $[0, 2\pi]$, respectively.

In an analogous way, we apply the same ν -point Gauss-Legendre quadrature rule to compute the single integral $M_n := M(t_n, \mathbf{x}_{pn}, \mathbf{w}_n)$, which reads

$$M_n = \frac{1}{R} \int_0^R m \left(\mathbf{x}_{pn} + r \frac{\mathbf{w}_n}{\|\mathbf{w}_n\|} \right) dr \approx \frac{1}{R} \sum_{p=1}^{\nu} w_p m \left(\mathbf{x}_{pn} + r_p \frac{\mathbf{w}_n}{\|\mathbf{w}_n\|} \right). \quad (3.21)$$

The computation of the integral terms as in Eqs. (3.20) and (3.21) has to be intended just in case the integrand functions are regular. If a function is piecewise regular the tailored application of the quadrature rule consists of applying the formulas in each subregion of the integration domains where the integrand functions are actually smooth.

In [1] possible discontinuities of the kernels K_r and K_θ and of the function m are taken into account. Instead, here we will assume the kernels to be smooth, but we will deal with possible singularities of the functions c and m .

For example, if the field c is defined as

$$c(t, \mathbf{y}) = \begin{cases} c_1 & \text{if } y_1 \leq d, \\ c_2 & \text{otherwise,} \end{cases} \quad (3.22)$$

being $d < L$ and $c_1 \neq c_2$, and at time t_n the cell center $\mathbf{x}_{pn} = (x_{pn}^1, x_{pn}^2)^\top$ is such that $|x_{pn}^1 - d| < R$, the cell senses the discontinuity inside the sensing region $\mathcal{S}(\mathbf{x}_{pn})$. Setting $\nu = 3$ and $\bar{\nu} = 4$ for the sake of simplicity, and considering the case in which the discontinuity d is placed to the right of cell center, the nodes of the tailored quadrature formula for the computation of \mathbf{W}_n are shown in Fig. 3.5.

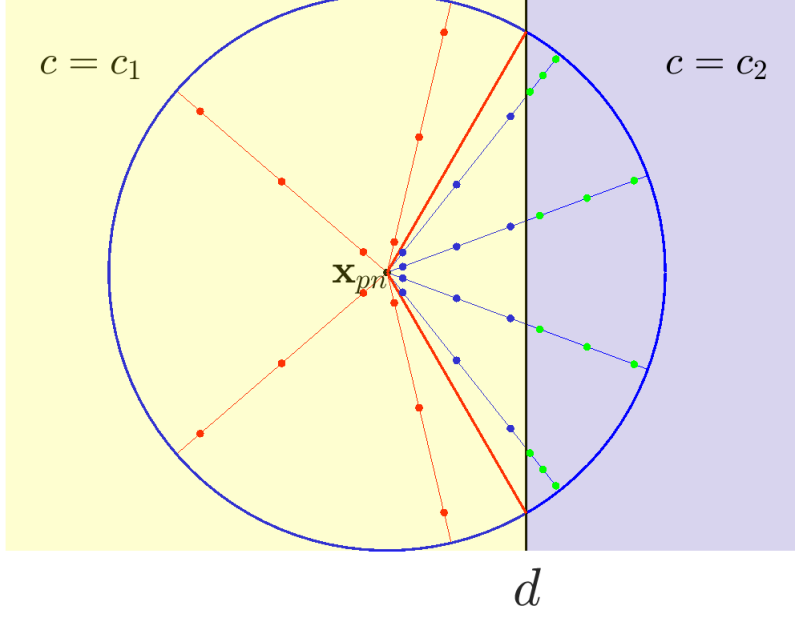


Figure 3.5: An example of quadrature nodes (blue, red, and green dots) used inside the sensing region $\mathcal{S}(\mathbf{x}_{pn})$ (blue circle) for the computation of \mathbf{W}_n if the field c is defined as in Eq. (3.22) and the cell senses the discontinuity to the right of its center.

For the sake of clarity, we write in the following the explicit computation of \mathbf{W}_n in the case mentioned above, that is if $x_{pn}^1 < d < x_{pn}^1 + R$. If $x_{pn}^1 - R < d < x_{pn}^1$ or if $x_{pn}^1 = d$ the computation can be easily generalized from this case, as well as the computation of M_n in case the field m has a vertical discontinuity as in Eq. (3.22), which are the only discontinuity we will take account of.

Referring to Fig. 3.5, being $\gamma := \arccos((x_{pn}^1 - d)/R)$ and $-\gamma$ the angles that individuate the discontinuity (red thick lines), the integral can be splitted as

$$\begin{aligned} \mathbf{W}_n &= \frac{c_1}{A} \int_0^R r K_r(r) \int_\gamma^{2\pi-\gamma} K_\theta \left(\mathbf{n}(\theta) \cdot \frac{\mathbf{w}_n}{\|\mathbf{w}_n\|} \right) \mathbf{n}(\theta) d\theta dr \\ &+ \frac{c_1}{A} \int_{-\gamma}^\gamma K_\theta \left(\mathbf{n}(\theta) \cdot \frac{\mathbf{w}_n}{\|\mathbf{w}_n\|} \right) \mathbf{n}(\theta) \int_0^{\bar{r}(\theta)} r K_r(r) dr d\theta \\ &+ \frac{c_2}{A} \int_{-\gamma}^\gamma K_\theta \left(\mathbf{n}(\theta) \cdot \frac{\mathbf{w}_n}{\|\mathbf{w}_n\|} \right) \mathbf{n}(\theta) \int_{\bar{r}(\theta)}^R r K_r(r) dr d\theta =: I_n^1 + I_n^2 + I_n^3, \end{aligned} \quad (3.23)$$

where the distance

$$\bar{r}(\theta) = \sqrt{(x_{pn}^1 - d)^2 + \left[(d - x_{pn}^1) \tan \theta\right]^2}, \quad \theta \in [-\gamma, \gamma], \quad (3.24)$$

individuates radially the jump of the field c .

Then, we use $\bar{\nu}$ nodes θ_q in the interval $[\gamma, 2\pi - \gamma]$ (red thin lines) and $\bar{\nu}$ nodes θ_q^* in the interval $[-\gamma, \gamma]$ (blue thin lines) and we denote with \bar{w}_q and \bar{w}_q^* the respective weights. For each angle θ_q we use ν nodes r_p and weights w_p in $[0, R]$ (red dots) because the field c is regular, computing

$$I_n^1 \approx \frac{c_1}{A} \left(\sum_{p=1}^{\nu} w_p r_p K_r(r_p) \right) \left(\sum_{q=1}^{\bar{\nu}} \bar{w}_q K_\theta \left(\mathbf{n}(\theta_q) \cdot \frac{\mathbf{w}_n}{\|\mathbf{w}_n\|} \right) \mathbf{n}(\theta_q) \right). \quad (3.25)$$

Instead, for each angle θ_q^* we use ν nodes in both intervals $[0, \bar{r}(\theta_q^*)]$ and $[\bar{r}(\theta_q^*), R]$. Denoting with r_p^* , w_p^* and with r_p^{**} , w_p^{**} the respective nodes and weights, we compute

$$I_n^2 \approx \frac{c_1}{A} \sum_{q=1}^{\bar{\nu}} \bar{w}_q^* K_\theta \left(\mathbf{n}(\theta_q^*) \cdot \frac{\mathbf{w}_n}{\|\mathbf{w}_n\|} \right) \mathbf{n}(\theta_q^*) \sum_{p=1}^{\nu} w_p^* r_p^* K_r(r_p^*), \quad (3.26)$$

and

$$I_n^3 \approx \frac{c_2}{A} \sum_{q=1}^{\bar{\nu}} \bar{w}_q^* K_\theta \left(\mathbf{n}(\theta_q^*) \cdot \frac{\mathbf{w}_n}{\|\mathbf{w}_n\|} \right) \mathbf{n}(\theta_q^*) \sum_{p=1}^{\nu} w_p^{**} r_p^{**} K_r(r_p^{**}). \quad (3.27)$$

3.2.3 Interpolation methods

As seen, the computation of the terms \mathbf{W}_n and M_n requires at each time step t_n the evaluation of the functions c and m on the proper quadrature nodes, but if the functions are not known in those points we need a proper interpolation process. We distinguish two different cases.

- If the functions c and m are known over the points \mathbf{y}_{ij} of a regular grid, a reasonable choice is to interpolate the unknown nodal values of with a bi-dimensional cubic spline, using not-a-knot conditions [6].
- If the functions c and m are known over the points $\hat{\mathbf{y}}_{ij}$ of a deformed grid due to the mechanical manipulation of the substrate, it is necessary to use interpolation methods that work on irregular grids. Among all possibilities, two choices are the *linear interpolation*, \mathcal{C}^0 continuous, and the *natural neighbor interpolation*, \mathcal{C}^1 continuous. Both methods are implemented in MATLAB[®] by the *scatteredInterpolant* function [52], and we refer to [53, 54] for details concerning theoretical results and their implementation, respectively.

We briefly review here these latter interpolation methods for a generic set of points in 2D, that we rename as \mathbf{x}_i , for $i = 1, \dots, n$, for the sake of simplicity.

The linear interpolation bases on a triangulation of the scattered data points, in which the value of the function to be interpolated at the generic point \mathbf{x} inside a triangle is given by the only plane that passes through the values known at its vertexes.

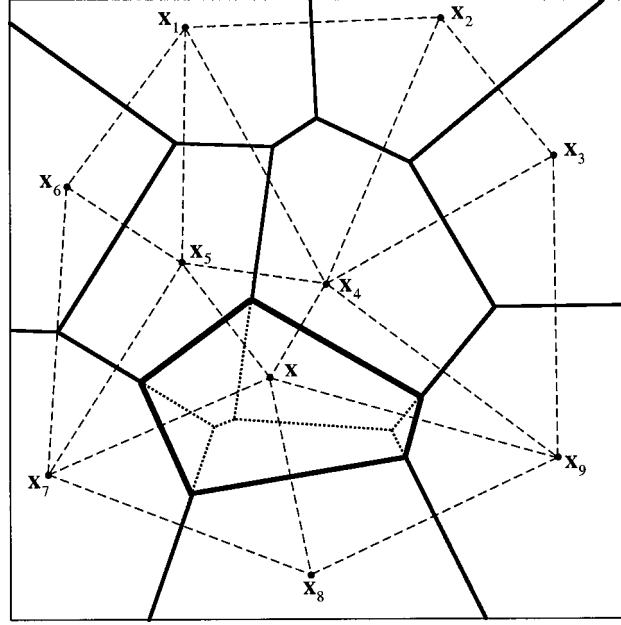


Figure 3.6: The Voronoi tiles of a scattered point set $\{\mathbf{x}_1, \dots, \mathbf{x}_9\}$, within the addition of a new point \mathbf{x} (see Eqs. (3.28), (3.29), (3.30)). Bold lines indicate the new tile of point \mathbf{x} ; the dotted lines inside it show the old tile boundaries before the addition of point \mathbf{x} . The Delaunay triangles associated with the Voronoi tessellation are also shown, indicated by thin dashed lines; the triangle edges are perpendicular bisectors of the tile edges. Figure reproduced from [54].

The natural neighbor interpolation method is based on the Voronoi tessellation of the given scattered point set. The Voronoi tessellation partitions the plane into a set of tiles (polygons), each tile T_i enclosing one point \mathbf{x}_i of the given point set. The tile T_i is defined as the area that is closer to the point \mathbf{x}_i than to any other scatter point, i.e.

$$T_i := \{\mathbf{x} \in \mathbb{R}^2 \mid \|\mathbf{x} - \mathbf{x}_i\| \leq \|\mathbf{x} - \mathbf{x}_j\| \forall j = 1, \dots, n\}. \quad (3.28)$$

Point \mathbf{x}_i of our point set is said to be a *natural neighbor* of point \mathbf{x}_j of the set if their respective tiles T_i and T_j have a common edge or point of contact.

Once the Voronoi tessellation of our point set has been constructed, all that we need in order to evaluate the interpolated value at a new point \mathbf{x} is simply to add \mathbf{x} to the set of scatter points, defining its new tile as

$$T(\mathbf{x}) := \{\mathbf{z} \in \mathbb{R}^2 \mid \|\mathbf{z} - \mathbf{x}\| \leq \|\mathbf{z} - \mathbf{x}_j\| \forall j = 1, \dots, n\}, \quad (3.29)$$

and its intersections with the old tiles as

$$T_i(\mathbf{x}) := T(\mathbf{x}) \cap T_i, \quad (3.30)$$

as shown in Fig. 3.6 in a representative case. Now, denoting the area of a tile T as $A(T)$,

the natural neighbor interpolant at the point \mathbf{x} could be defined as

$$\hat{f}(\mathbf{x}) = \sum_{i \text{ neigh}} h_i(\mathbf{x}) z_i, \quad (3.31)$$

where

$$h_i(\mathbf{x}) := \frac{A(T_i(\mathbf{x}))}{A(T(\mathbf{x}))}, \quad z_i := f(\mathbf{x}_i), \quad (3.32)$$

and the sum is intended only over the natural neighbors of \mathbf{x} .

The interpolant of Eq. (3.31) is only \mathcal{C}^0 continuous, since its derivatives are discontinuous at the points \mathbf{x}_i . In order to obtain a \mathcal{C}^1 continuous interpolant we must take into account also the gradient at each of the points. It can be shown that in this case the interpolant reads

$$\hat{f}(\mathbf{x}) = \sum_{i \text{ neigh}} w_i(\mathbf{x}) g_i(\mathbf{x}), \quad (3.33)$$

where

$$w_i(\mathbf{x}) := \frac{\frac{h_i(\mathbf{x})}{\|\mathbf{x} - \mathbf{x}_i\|}}{\sum_{j \text{ neigh}} \frac{h_j(\mathbf{x})}{\|\mathbf{x} - \mathbf{x}_j\|}}, \quad g_i(\mathbf{x}) := z_i + \nabla z(\mathbf{x}_i) \cdot (\mathbf{x} - \mathbf{x}_i), \quad (3.34)$$

and where $\nabla z(\mathbf{x}_i)$ is an estimate value of the gradient of the underlying function $z(\mathbf{x})$ at point \mathbf{x}_i . All sums are intended over the natural neighbors of \mathbf{x} .

Chapter 4

Numerical simulations

After the presentation of the complete model and the analysis of the numerical issues, in this Chapter we finally show some numerical simulations performed for both processes of durotaxis and tensotaxis. Before that, we choose all the parameters and the kernels involved in the equations, as well as the numerical parameters and methods that preserve the overall accuracy and computational cost for the cell migration model.

4.1 Parameters and kernels K_r and K_θ

We refer to [1] to set the parameter involved in the cell migration model. The length of the squared domain $\Omega = [0, L] \times [0, L]$ is $L = 700 \mu\text{m}$, whereas the extension of cell protrusions R is assumed equal to $20 \mu\text{m}$. The representative cell is able to reach a maximum speed of $V_{max} = 0.009 \mu\text{m/s}$ and to re-orient in a period τ equal to 300 s (see Eqs. (3.12) and (3.9), respectively). The Michaelis–Menten constant ε in Eq. (3.9) is fixed to 0.001 . All the other parameters involved will be specified in the proper sections; in particular we remark that the final time T will be chosen to avoid that the cell (as well as its sensing region) reaches the domain boundaries.

Concerning the choice of the kernels K_r and K_θ in Eq. (3.10), we remind that they measure the capacity of the cell to sense the field c in a non-local and non-isotropic way on the individual sensing region. The choice of these kernels must therefore take account of the reason why the cell migrates, i.e. which are the stimuli perceived by the cell and how the cell perceives them.

As already outlined, in [1] the field c is the concentration of a chemoattractant, so the cell moves due to chemotaxis. In that case it is reasonable to consider K_r a decreasing function, since the cell perceives the chemoattractant less intensely as the distance from its center of mass increases. Instead, we hypothesize that the local amount of mechanical receptors increases with the distance from the cell center, since integrins and FAs assemble and disassemble with a higher rate at the end of cell protrusions [8]. Among all the possible choices, we set

$$K_r(r) = -2 \left(\frac{r}{R} \right)^3 + 3 \left(\frac{r}{R} \right)^2, \quad \text{for } r \in [0, R], \quad (4.1)$$

which is nothing but increasing (in its domain) degree 3 polynomial with the conditions

$$K_r(0) = 0, \quad K_r(R) = 1, \quad K_r'(0) = K_r'(R) = 0, \quad (4.2)$$

and it is shown in Fig. 4.1. We recall that r is the distance from the cell center of mass.

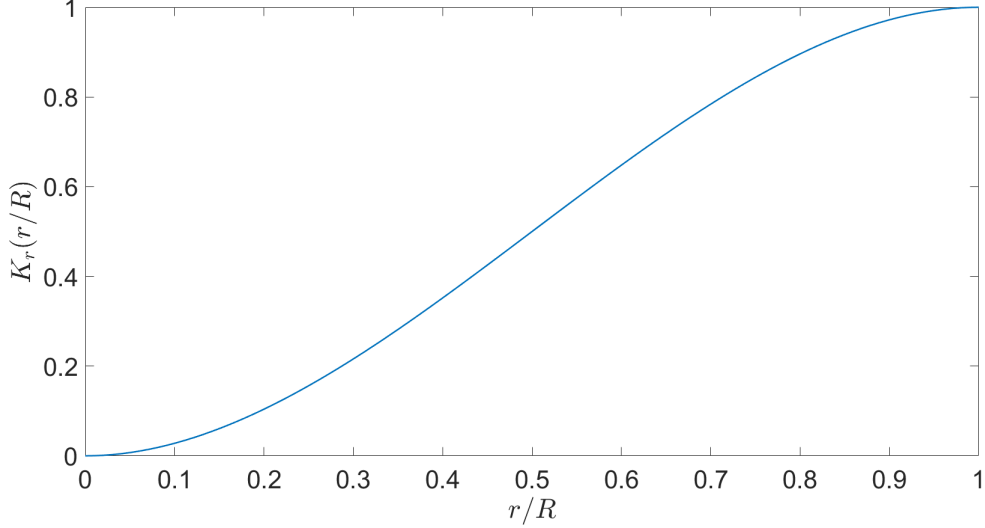


Figure 4.1: Kernel K_r defined in Eq.(4.1) and used for the computation of cell preferred direction of motion in Eq. (3.10).

For what concerns the choice of $K_\theta(u)$, where $u = \mathbf{n}(\theta) \cdot \mathbf{w} / \|\mathbf{w}\|$ is the scalar product between the vector $\mathbf{n}(\theta) = (\cos \theta, \sin \theta)$ (with $\theta \in [0, 2\pi)$) and the normalized polarization $\mathbf{w} / \|\mathbf{w}\|$, we consider two different possibilities:

1. we assume that the amount of receptors is higher towards cell's front than toward its tail, and consistently we take

$$K_\theta(u) = -\frac{1}{4}u^3 + \frac{3}{4}u + \frac{1}{2}, \quad \text{for } u \in [-1,1], \quad (4.3)$$

so that the cell is biased to migrate towards its actual direction of motion. In the following we will refer to (4.3) as “biased kernel”;

2. we assume that the amount of receptors is the same towards the cell's head and tail and gradually vanishes, taking

$$K_\theta(u) = u^{2k_1}, \quad \text{for } u \in [-1,1], \quad (4.4)$$

with $k_1 \in \mathbb{N} \setminus \{0\}$. If this is the case, the cell does not distinguish between its head or tail for the choice of its preferred axis. For example, if the field c is constant over the circular sensing region, with the latter choice of K_θ the integral \mathbf{W} in Eq. (3.10) vanishes, and this leads $\|\mathbf{w}(t)\|$ to rapidly decrease to zero. In the following we will refer to (4.4) as “unbiased kernel”.

We plotted both kernels K_θ of Eqs. (4.3) and (4.4) in Fig. 4.2. In the following we will consider $k_1 = 1$.

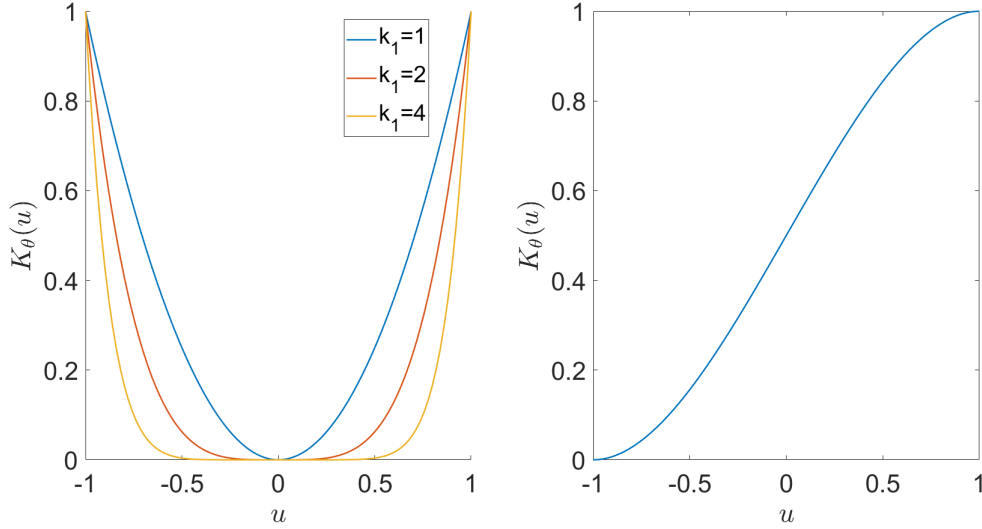


Figure 4.2: Different choices for the kernel K_θ used for the computation of cell preferred direction of motion in Eq. (3.10). The “unbiased kernel” defined in Eq. (4.4) is shown on the left for $k_1 \in \{1,2,4\}$, whereas the “biased kernel” defined in Eq. (4.3) is shown on the right.

4.2 Validation and choice of the numerical methods

The numerical approach for the cell migration model proposed in Section 3.2 has already been validated in [1] if the fields c and m are known analytically or they are defined over a regular grid. In particular, the choice of discretization parameters Δt and Δy sufficiently small leads to the theoretical quadratic order of convergence of the Heun method and the linear order of convergence of the Euler method when the spline interpolation is considered.

If a deformation of the grid occurs, as outlined in Subsection 3.2.3, we need different interpolation methods. Here, we aim to understand if it is possible to obtain the theoretical orders of convergence of both methods when coupled with a linear interpolation or natural neighbor interpolation. With this purpose, we set the same benchmark test as in [1], defining the following test field as

$$c(t, \mathbf{y}) = c_0 \frac{e^{y_1/\sqrt{\delta}} - e^{(2L-y_1)/\sqrt{\delta}}}{1 - e^{2L/\sqrt{\delta}}}, \quad (4.5)$$

with $c_0 = 0.027 \mu\text{M}$ and $\delta = 33250 \mu\text{m}^2$, and the ECM protein density as

$$m(t, \mathbf{y}) = \begin{cases} 0.75 & \text{if } y_1 \leq L/2, \\ 0.5 & \text{otherwise.} \end{cases} \quad (4.6)$$

We assume the explicit form of the kernels K_r and K_θ as in Eqs. (4.1) and (4.3), respectively, we define the function f of Eq. (3.12) as

$$f(M) = 4M(1 - M) \quad (4.7)$$

(the justification for this choice will be given in Section 4.3), and we set $\mathbf{x}_p(0) = (3/4L, L/4)$, $\mathbf{w}(0) = (0,1)$ as initial conditions, and the final time $T = 16$ h.

We assume as reference trajectory the solution obtained with $\bar{N} = 3200$ time-steps, and we consider a sequence of approximated cell trajectories obtained with N time steps. To easily compare the resulting approximated trajectories with the reference one, we require that N is a divisor of \bar{N} (i.e., there exists $k \in \mathbb{N}$ such that $\bar{N} = kN$). We then introduce the relative error

$$\text{err}_{\mathbf{x}}^{N,\Lambda} := \max_{n=0,\dots,N} \frac{\|\bar{\mathbf{x}}_{kn} - \mathbf{x}_n^\Lambda\|}{\|\bar{\mathbf{x}}_{kn}\|}, \quad (4.8)$$

where \mathbf{x}_n^Λ with $n = 0, \dots, N$, denotes the approximated cell trajectory obtained by applying, at any time step, $\nu = \bar{\nu} = 16$ nodes for the computation of the integral terms, and by replacing the variable c either with its linear or its natural neighbor interpolation, assuming that the field c is known over a regular grid with $\Delta y = L/\Lambda$. Conversely, $\bar{\mathbf{x}}_{kn}$, with $n = 0, \dots, \bar{N}$, denotes the reference solution obtained by dividing the period of observation into $\bar{N} = kN = 3200$ time steps, and by using $\nu = \bar{\nu} = 32$ nodes and the analytic expression of c for the quadrature nodes. In denoting cell trajectories we suppressed the subscript p for simplicity. The reference trajectory, as well as the fields defined in Eqs. (4.5) and (4.6), is shown in Fig. 4.3.

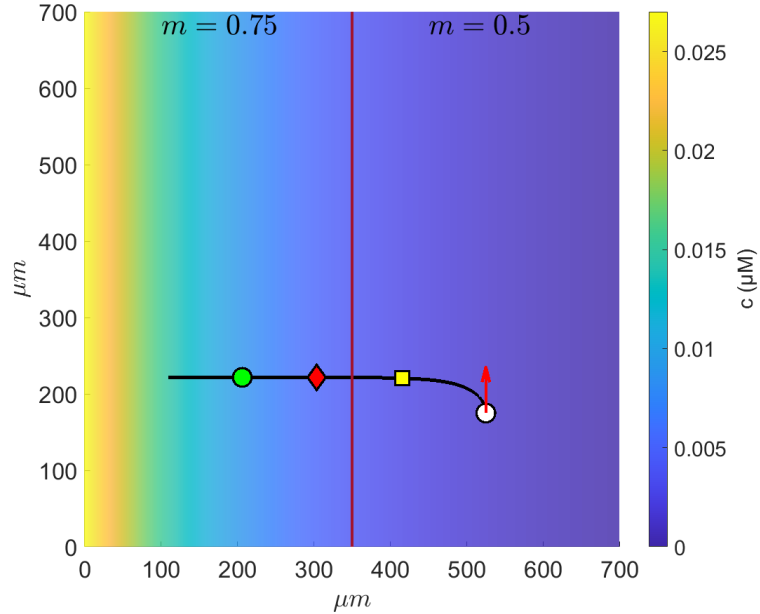


Figure 4.3: Reference trajectory of a cell initially located at $\mathbf{x}_p(0) = (3/4L, L/4)$ (white circle) and with $\mathbf{w}(0) = (0,1)$ (red arrow), computed with $\bar{N} = 3200$ time-steps and $T = 16$ h. The fields c and m are defined in Eqs. (4.5) and (4.6), respectively, and the kernels K_r and K_θ in Eqs. (4.1) and (4.3), respectively. The colored symbols denote the position at the instants $T/4$ (yellow square), $T/2$ (red diamond), $3T/4$ (green circle).

Finally, we compute the estimated order of convergence as

$$\text{EOC}^\Lambda := \log_2 \left(\text{err}_x^{N,\Lambda} / \text{err}_x^{2N,\Lambda} \right). \quad (4.9)$$

For $N \in \{100, 200, 400, 800, 1600\}$ and $\Lambda \in \{20, 40, 80\}$, the results are shown in Tables 4.1 and 4.2 for Euler method coupled with linear and natural neighbor interpolation, respectively, and in Tables 4.3 and 4.4 for Heun method coupled with linear and natural neighbor interpolation, respectively.

N	$\text{err}_x^{N,20}$	EOC^{20}	$\text{err}_x^{N,40}$	EOC^{40}	$\text{err}_x^{N,80}$	EOC^{80}
100	3.44e-03		3.66e-03		3.64e-03	
		1.16		1.07		1.07
200	1.54e-03		1.75e-03		1.73e-03	
		0.78		1.09		1.11
400	8.96e-04		8.19e-04		8.01e-04	
		0.29		1.18		1.22
800	7.31e-04		3.62e-04		3.43e-04	
		0.06		1.42		1.56
1600	7.01e-04		1.36e-04		1.16e-04	

Table 4.1: Relative error $\text{err}_x^{N,\Lambda}$ defined in Eq. (4.8) and estimated order of convergence EOC^Λ given in Eq. (4.9) for the solution of the benchmark test defined in Section 4.2 obtained with Euler method coupled with a linear interpolation.

N	$\text{err}_x^{N,20}$	EOC^{20}	$\text{err}_x^{N,40}$	EOC^{40}	$\text{err}_x^{N,80}$	EOC^{80}
100	3.41e-03		3.65e-03		3.64e-03	
		1.19		1.07		1.07
200	1.50e-03		1.74e-03		1.73e-03	
		1.00		1.10		1.11
400	7.49e-04		8.14e-04		8.00e-04	
		-0.22		1.19		1.22
800	8.74e-04		3.57e-04		3.43e-04	
		-0.15		1.36		1.57
1600	9.70e-04		1.39e-04		1.16e-04	

Table 4.2: Relative error $\text{err}_x^{N,\Lambda}$ defined in Eq. (4.8) and estimated order of convergence EOC^Λ given in Eq. (4.9) for the solution of the benchmark test defined in Section 4.2 obtained with Euler method coupled with a natural neighbor interpolation.

The values reported in Tables 4.1 and 4.2 show that the estimated order of convergence of Euler method coincides with the linear theoretical order if the spatial discretization parameter is at least 40. For what concerns Heun method, from Tables 4.3 and 4.4 we notice that the parameter $\Lambda = 80$ is not sufficient to recover the quadratic order of the

N	$\text{err}_{\mathbf{x}}^{N,20}$	EOC^{20}	$\text{err}_{\mathbf{x}}^{N,40}$	EOC^{40}	$\text{err}_{\mathbf{x}}^{N,80}$	EOC^{80}
100	5.37e-04		4.75e-04		4.43e-04	
		-0.55		2.47		1.94
200	7.86e-04		8.58e-05		1.16e-04	
		0.12		1.21		2.20
400	7.22e-04		3.72e-05		2.52e-05	
		0.04		-0.53		2.82
800	7.04e-04		5.37e-05		3.56e-06	
		0.01		-0.14		-0.74
1600	6.99e-04		5.92e-05		5.95e-06	

Table 4.3: Relative error $\text{err}_{\mathbf{x}}^{N,\Lambda}$ defined in Eq. (4.8) and estimated order of convergence EOC^Λ given in Eq. (4.9) for the solution of the benchmark test defined in Section 4.2 obtained with Heun method coupled with a linear interpolation.

N	$\text{err}_{\mathbf{x}}^{N,20}$	EOC^{20}	$\text{err}_{\mathbf{x}}^{N,40}$	EOC^{40}	$\text{err}_{\mathbf{x}}^{N,80}$	EOC^{80}
100	1.06e-03		5.00e-04		4.42e-04	
		0.23		3.12		1.83
200	9.04e-04		5.77e-05		1.24e-04	
		-0.14		-0.87		1.88
400	9.95e-04		1.06e-04		3.37e-05	
		-0.03		-0.28		1.74
800	1.02e-03		1.28e-04		1.00e-05	
		0.01		-0.07		1.08
1600	1.02e-03		1.34e-04		4.76e-06	

Table 4.4: Relative error $\text{err}_{\mathbf{x}}^{N,\Lambda}$ defined in Eq. (4.8) and estimated order of convergence EOC^Λ given in Eq. (4.9) for the solution of the benchmark test defined in Section 4.2 obtained with Heun method coupled with a natural neighbor interpolation.

method, that must be satisfied for every choice of N . Although a further analysis with higher values of Λ, N, \bar{N} might be possible to check whether it is possible to recover the theoretical quadratic order, for the purposes of this Thesis we will restrict to use Euler method coupled with a linear interpolation if a deformation of the grid occurs, being sure that at least the linear order is guaranteed.

Summing up, having in mind that a sufficiently accurate approximation of the cell trajectory is reasonably identified by a relative error approximatively $1.0\text{e-}03$, in the following numerical simulations we will consider:

- Heun method if the fields c and m are known analitically;
- Euler method coupled with a linear interpolation if the fields c and m are known over a deformed grid, with $\Lambda = 70$ in the correspondent undeformed grid.

Unless otherwise specified, in both cases we will use $\nu = \bar{\nu} = 16$ quadrature nodes and we will set $T = 16$ h and $N = 100$ time steps (or $T = 32$ h and $N = 200$), which correspond to a time discretization parameter $\Delta t = 576$ s.

4.2.1 Addition of a random term in cell direction

Once the numerical approach has been validated and the numerical parameter has been set, we aim to simulate the cell migration process in response to mechanical stimuli. However, the model presented so far is purely deterministic and does not account for a Brownian crawling, typical of biological individuals. We aim to consider this process too, in order to simulate more realistic trajectories, having in mind that the analytical results of [1] do not hold in this case.

We may add then a random term to the discretized equation of evolution of the cell center (3.8), i.e. we may redefine the right hand side of the equation at time t_n as

$$\mathbf{g}_x(t_n, \mathbf{x}_{pn}, \mathbf{w}_n) = v(t_n) \mathbf{w}_n + \eta_n \mathbf{q}_n, \quad (4.10)$$

where the random direction \mathbf{q}_n is defined as

$$\mathbf{q}_n = \begin{pmatrix} \cos \alpha_{t_n} \\ \sin \alpha_{t_n} \end{pmatrix}, \quad (4.11)$$

being α_{t_n} a different realization of a random variable uniformly distributed in $[0, 2\pi)$ at each time step. The parameter η_n measures the magnitude of this random effect, and to be consistent with the model it is reasonable to consider $\eta_n \in [\eta_{min}, V_{max}]$, being V_{max} the maximum cell speed defined in Eq. (3.12) and $\eta_{min} > 0$ to be defined. In particular, we choose to model η_n as a linear function of $\|\mathbf{w}_n\|$, taking into account that if at time t_n the cell is fully polarized, i.e. $\|\mathbf{w}_n\| = 1$, the random effect reaches its minimum, and vice versa. Then, its definition reads

$$\eta_n = V_{max} - (V_{max} - \eta_{min}) \|\mathbf{w}_n\|. \quad (4.12)$$

In the following numerical simulations we will always specify whether we will take account of this additional random term or not, and we will set $\eta_{min} = 0.3V_{max}$. It is worthwhile to outline that if the random term is added to the model the solution is not unique anymore. However, with this choice of η_n , we expect to have a trajectory qualitatively similar to the case without the random term if the cell is almost completely polarized, while we expect a random Brownian crawling if the cell is not polarized.

4.3 Durotaxis

In this Section we aim to simulate the process of durotaxis. As outlined in Chapter 1, cells can sense the rigidity of the substrate they are anchored on and move towards stiffer regions. The simplest choice of the field c , the quantity that the cell senses to identify a preferred direction of locomotion, is then the *stiffness distribution* on the substrate

$$c(t, \mathbf{y}) = E(\mathbf{y}). \quad (4.13)$$

On the other hand, the field m is related to cell motility and a reasonable choice is to follow the chemotactic model of [1] considering the *local fraction of ECM proteins*, that influences the retraction/expansion cycles of cell motility structures. Within this context, the function f in Eq. (3.12) is modeled as

$$f(M) = 4M(1 - M), \quad (4.14)$$

where M has been defined in Eq. (3.11). This assumption is consistent since at low density of matrix elements (i.e., $M \approx 0$), the cell is unable to find sufficient protein sites to hold onto and to use for traction, being therefore unable to significantly displace. At the other extremum, an abundance of ECM proteins (i.e., $M \approx 1$) typically leads to the formation of stable focal adhesions and, hence, to low detachment and migration rates. Intermediate amounts of ECM densities instead result in optimal attachment–detachment cycles and maximal cell speed (i.e., $M \approx 0.5$). The parabola of Eq. (4.14) is shown in Fig. 4.4.

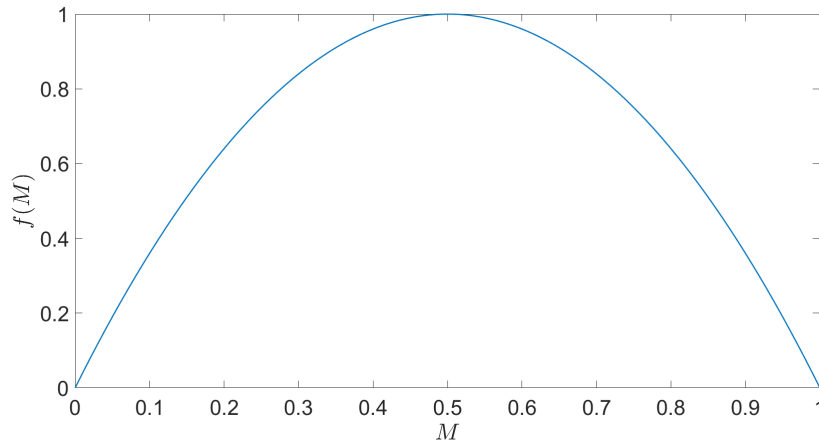


Figure 4.4: Function f defined in Eq. (4.14) and used in Eq. (3.12) for the constitutive relation of cell motility.

Since the fields E (or c , equivalently) and m will be analytically defined, as outlined in Section 4.2 we will compute the solution using Heun method and setting the final time $T = 16$ h and using $N = 100$ time-steps (or $T = 32$ h and $N = 200$). Furthermore, the choice of a piecewise constant rigidity and of the polynomial kernel K_r of degree 3 in Eq. (4.1) allows us to use just $\nu = 3$ quadrature nodes for the computation of \mathbf{W} along the radial direction. In fact, the Gauss-Legendre quadrature formula ensures the exact integration of the 4 degree polynomial

$$\int_a^b r K_r(r) dr \quad (4.15)$$

with 3 nodes [6], whether if the integration interval is $[0, R]$ as in Eq. (3.25), or $[0, \bar{r}(\theta_q^*)]$ as in Eq. (3.26), or $[\bar{r}(\theta_q^*), R]$ as in Eq. (3.27).

4.3.1 Piecewise constant rigidity

Several authors considered a piecewise constant rigidity defined on the substrate to test their durotactic models [8, 9, 18, 33], also because this setup is used for biological experiments [2, 14]. We will consider a setup in which a strip of stiffer substrate is placed between two softer sides of substrate. That is, we define the substrate rigidity as

$$E(\mathbf{y}) = \begin{cases} E_1 & \text{if } L/2 - d \leq y_1 \leq L/2 + d, \\ E_2 & \text{otherwise,} \end{cases} \quad (4.16)$$

with $d = 50 \mu\text{m}$, and we set $E_1 = 30 \text{ kPa}$ and $E_2 = 13 \text{ kPa}$ as in [2]. The distribution of the fixed ECM substance reads arbitrarily

$$m(t, \mathbf{y}) = \begin{cases} 0.5 & \text{if } L/2 - d \leq y_1 \leq L/2 + d, \\ 0.75 & \text{otherwise,} \end{cases} \quad (4.17)$$

so that the cell move faster on the stiffer side of the substrate. We investigate the solution with initial conditions

$$\mathbf{x}_p(0) = (450, 450) \mu\text{m}, \quad \mathbf{w}(0) = \left(-\frac{\sqrt{2}}{2}, -\frac{\sqrt{2}}{2} \right). \quad (4.18)$$

We firstly investigate the choice of the “biased kernel” K_θ as in Eq. (4.3), so that the cell is biased to move towards its actual direction of polarization. The left panel of Fig. 4.5 shows the solution obtained with no additional random term, while the right panel shows a solution with the additional random term as explained in Subsection 4.2.1. Furthermore, in Fig. 4.6 we show 10 different trajectories with the addition of the random term, all with the same parameters and initial conditions. Without the additional random term, we notice that the cell’s trajectory is nearly straight, with changes in direction as the cell senses the stiffness discontinuity within its sensing region. In particular, once the cell enters the stiffer substrate strip, it continues its motion without returning to the softer part. With the additional random term the behaviour is qualitatively the same, with less regular trajectories.

If we set the “unbiased kernel” K_θ as in Eq. (4.4), neither the kernels nor the stiffness field induce a polarization of the cell. Thus, as outlined in Section 4.1, without the random term the norm $\|\mathbf{w}(t)\|$ rapidly decreases to zero and the displacement of the cell is almost null. Instead, with the addition of the random term a small value of $\|\mathbf{w}(t)\|$ leads the parameter η_n in Eq. (4.12) to a value near to the maximum cell speed V_{max} , and thus the cell begins to move randomly. The results in Fig. 4.7 show that if the cell senses the stiffness discontinuity within its sensing region, it moves rapidly towards the stiffer strip and continues there the Brownian crawling. For the sake of clarity, we placed the cell at different initial position (with the same distance from the stiffness discontinuity) in order to avoid overlapping trajectories.

4.3.2 Regular smooth rigidity

Another setup we may consider is a regular rigidity field, varying between the two values E_1 and E_2 from one side of the substrate to the other. The simplest assumption is a linear

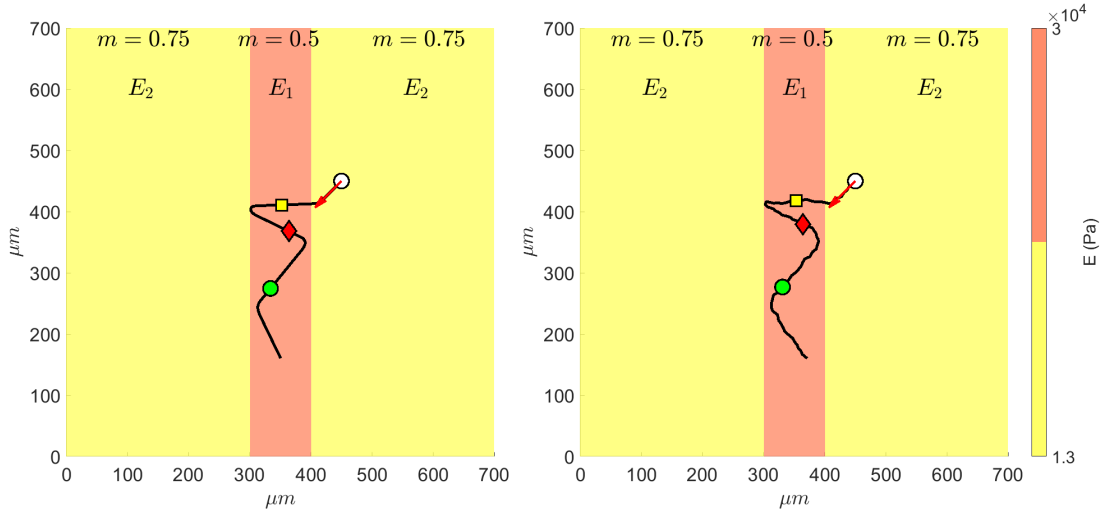


Figure 4.5: Solution with initial conditions set in Eq. (4.18) (white circle and red arrow), computed with $N = 100$ time-steps and $T = 16$ h. The fields c (or E) and m are defined in Eqs. (4.16) and (4.17), respectively, and the kernels K_r and K_θ in Eqs. (4.1) and (4.3), respectively. The colored symbols denote the position at the instants $T/4$ (yellow square), $T/2$ (red diamond), $3T/4$ (green circle). On the left, the solution without the random term. On the right, the solution with the additional random term defined in Subsection 4.2.1.

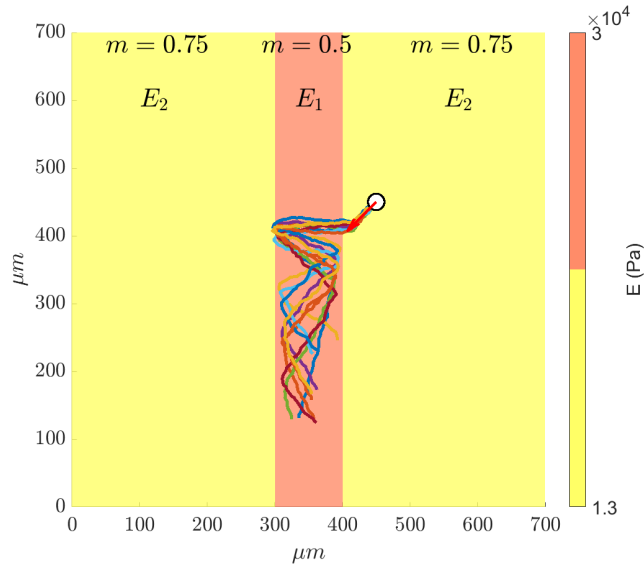


Figure 4.6: 10 different trajectories solutions of the problem set as on the right panel of Fig. 4.5.

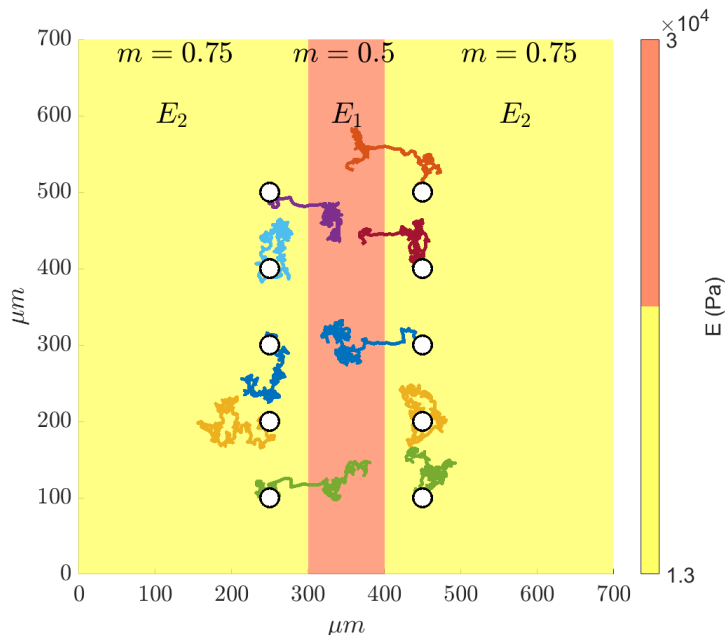


Figure 4.7: 10 different trajectories computed with $N = 200$ time-steps and $T = 32$ h. The fields c (or E) and m are defined in Eqs. (4.16) and (4.17), respectively, and the kernels K_r and K_θ in Eqs. (4.1) and (4.4), respectively. The white circles are the initial positions of the cell, that are always placed $50 \mu\text{m}$ from the stiffness discontinuity.

variation [33], i.e. we define

$$E(\mathbf{y}) = \frac{E_1 - E_2}{L} y_1 + E_2. \quad (4.19)$$

Having no precise biological justification for the relation between ECM density and substrate stiffness, in this case we assume a uniform field $m(t, \mathbf{y}) = 0.5$ for any t and \mathbf{y} , having in mind that a different choice results in a slowdown of the cell.

We investigate the solution with initial conditions

$$\mathbf{x}_p(0) = (100, 200) \mu\text{m}, \quad \mathbf{w}(0) = (0, 1), \quad (4.20)$$

and we show in Fig. 4.8 and 4.9 the results for the “biased kernel” K_θ as defined in Eq. (4.3), and in Fig. 4.10 and 4.11 the results for the “unbiased kernel” K_θ as defined in Eq. (4.4). Within the stiffness field defined in Eq. (4.19) the cell is almost fully polarized, so that with the additional random term the trajectory is qualitatively similar. Finally, we note that the choice of the kernel K_θ as in Eq. (4.4) makes the choice of initial polarization irrelevant, since the cell immediately polarizes to the right following the linear field of stiffness.

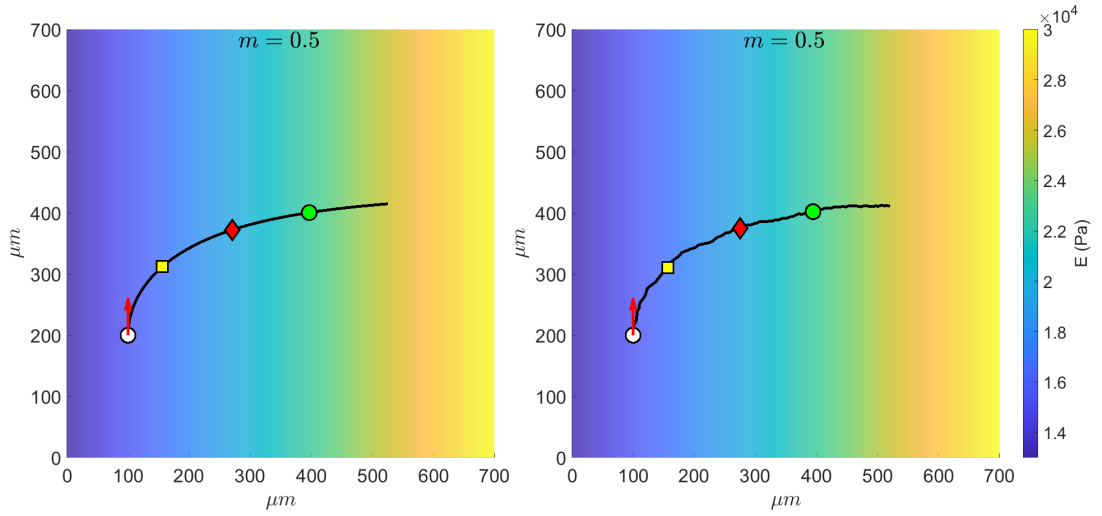


Figure 4.8: Solution with initial conditions set in Eq. (4.20) (white circle and red arrow), computed with $N = 100$ time-steps and $T = 16$ h. The field c (or E) is defined in Eq. (4.19), while we set $m = 0.5$ uniformly. The kernels K_r and K_θ are defined in Eqs. (4.1) and (4.3), respectively. The colored symbols denote the position at the instants $T/4$ (yellow square), $T/2$ (red diamond), $3T/4$ (green circle). On the left, the solution without the random term. On the right, the solution with the additional random term defined in Subsection 4.2.1.

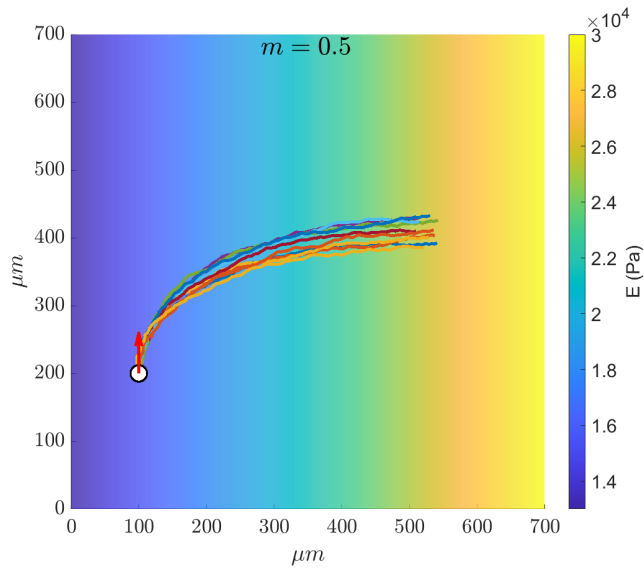


Figure 4.9: 10 different trajectories solutions of the problem set as on the right panel of Fig. 4.8.

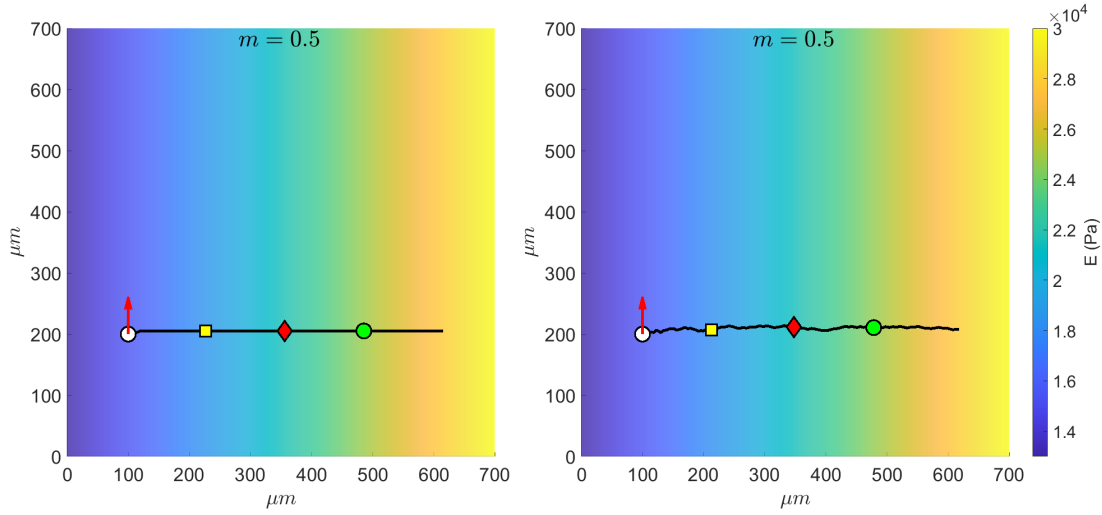


Figure 4.10: Solution with initial conditions set in Eq. (4.20) (white circle and red arrow), computed with $N = 100$ time-steps and $T = 16$ h. The field c (or E) is defined in Eq. (4.19), while we set $m = 0.5$ uniformly. The kernels K_r and K_θ are defined in Eqs. (4.1) and (4.4), respectively. The colored symbols denote the position at the instants $T/4$ (yellow square), $T/2$ (red diamond), $3T/4$ (green circle). On the left, the solution without the random term. On the right, the solution with the additional random term defined in Subsection 4.2.1.

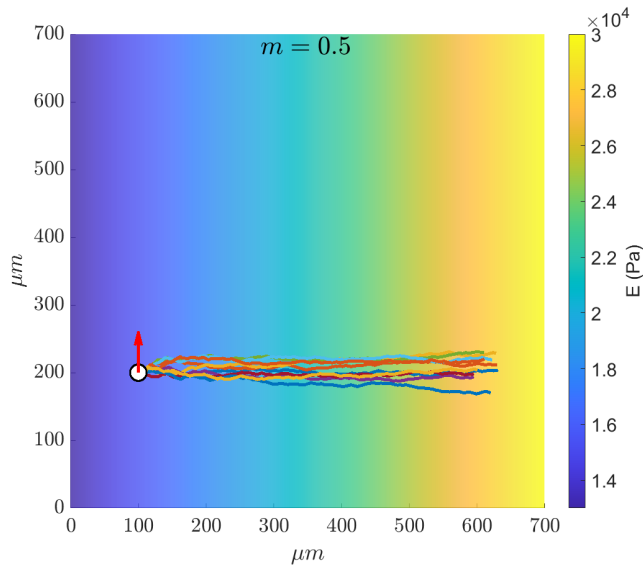


Figure 4.11: 10 different trajectories solutions of the problem set as on the right panel of Fig. 4.10.

4.4 Tensotaxis

In this Section we aim to simulate the process of tensotaxis, that is the migration of cells towards tensile stresses and away from compressive stresses induced on the substrate. As outlined in Section 1.2, several models have been proposed in literature to study and reproduce this phenomenon. In our model all the stimuli the cell senses must be included in the fields c and m . In particular the cell must sense whether the substrate is either pushed away from it or pulled towards it, and must migrate in response to this information. We choose to include this information in the field c and we set c to be equal to the *first invariant of the stress tensor* introduced in Eq. (2.43), that is a scalar measure of the mean stress applied to the substrate, i.e.

$$c = \text{tr } \mathbb{T} = \text{tr} \left(J^{-1} \mathbb{P} \mathbb{F}^T \right). \quad (4.21)$$

Thus, a positive value of the stress corresponds to a tensile stress, and the cell is attracted by it, whereas a negative value corresponds to a compressive stress and the cell is repelled from it.

For what concerns cell motility, a reasonable choice is to link m to the *strain energy density* stored by the substrate when stretched [3], so that the cell velocity increases if it is in a region with a high level of energy, both if the substrate is pulled or pushed. Taking into account that the function m must assume values in $[0,1]$ for modelistic reasons as explained in Section 2.1, we choose

$$m(t, \mathbf{y}) = \frac{W(\mathbf{y})^{1/k_2}}{\max_{\mathbf{y} \in \Omega} \left[W(\mathbf{y})^{1/k_2} \right]}, \quad (4.22)$$

where $k_2 \geq 1$ and W is the strain energy density function defined either in Eq. (2.56) if we assume a non-linear behavior of the substrate, or in Eq. (2.60) if the response is considered linear. We consider the exponent $1/k_2$ because, within the mechanical load we deal with, the energy is extremely localized in the region \mathcal{D} in which the load is applied, and the cell would not sense it properly. We assume $k_2 = 2$ and we show qualitatively the differences between the fields W and $W^{1/2}$ in a representative case in Fig. 4.12.

The function f in Eq. (3.12) has to be modeled taking into account that the velocity is large if the cell is in a region with a high level of energy. We choose to introduce a minimal cell speed $v_{min} \in [0, V_{max})$ and we define

$$f(M) = (2v_{min} - 2)M^3 + (3 - 3v_{min})M^2 + v_{min}. \quad (4.23)$$

We may note that f is nothing but a degree 3 polynomial with the conditions

$$f(0) = v_{min}, \quad f(1) = 1, \quad f'(0) = f'(1) = 0, \quad (4.24)$$

as shown in Fig. 4.13, similarly as done in the choice of the kernels K_r and K_θ in Eqs. (4.1) and (4.3).

With these assumptions we model the cell to have a minimal speed v_{min} even if it does not perceive any energy, the speed increases monotonically as the amount of energy

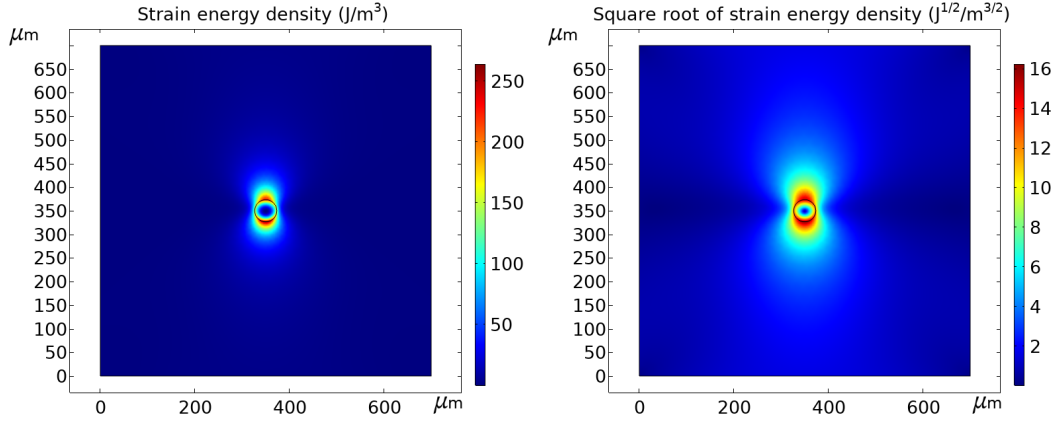


Figure 4.12: Qualitative differences between the substrate strain energy density (on the left) and its square root (on the right) in a representative case, in Lagrangian coordinates.

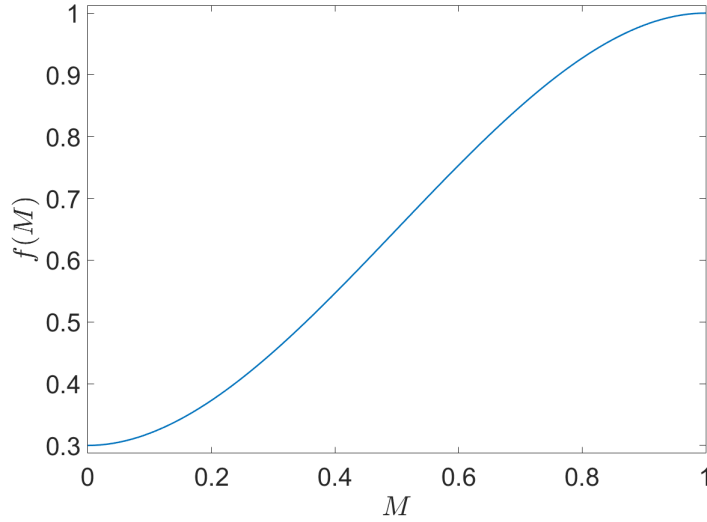


Figure 4.13: Function f defined in Eq. (4.23) for $v_{min} = 0.3V_{max}$ and used in Eq. (3.12) for the constitutive relation of cell motility.

perceived increases, and it reaches the maximal value V_{max} when the strain energy reaches its maximum. In the following we will consider $v_{min} = 0.3V_{max}$.

Furthermore, for the solution of the mechanical problem we fix the substrate thickness in Eqs. (3.1) and (3.5) as $h = 35 \mu\text{m}$ [4, 5, 16].

Since the fields c and m will not be analytically defined, but they will be known on a deformed grid with $\Lambda = 70$, as outlined in Section 4.2 we will compute the solution using Euler method coupled with a linear interpolation, setting the final time $T = 16$ h and using $N = 100$ time-steps (or $T = 32$ h and $N = 200$).

4.4.1 Differences in substrate’s mechanical behaviour

First of all we aim to outline the differences between a linear or non-linear behaviour of the substrate. Following the relation proposed in [4] we fix the material constant of the energy defined in Eq. (3.3)

$$c_2 = 0, \quad c_4 = \frac{2c_1(1 + \nu)}{3(1 - 2\nu)}, \quad (4.25)$$

where ν is the Poisson ratio, which is assigned the value $\nu = 0.48$ due to the quasi-incompressibility of polyacrylamide gels (PAG) [5]. Furthermore, in [4] it is shown that the coefficient c_1 is related to the linear behaviour of the substrate, in the sense that we can approximate its Young modulus as

$$E \approx 6c_1, \quad (4.26)$$

whereas c_3 is linked to the non-linear response. This information is helpful to compare the different responses of the substrate.

Besides, as mentioned in Section 2.2, the coefficients c_1 and c_3 are related to the concentrations of acrylamide and bis-acrylamide of the gel. In [4] the concentration of acrylamide is 10% and the concentration of bis-acrylamide changes between 0.03% and 0.1%, giving the values of the coefficient c_1 and c_3 as shown in Table 4.5.

$[Bis]$ (%)	c_1 (kPa)	c_3 (kPa)	E (kPa)
0.10	4.66 ± 0.88	5.40 ± 4.80	27.96 ± 5.28
0.05	2.48 ± 0.28	2.50 ± 1.10	14.88 ± 1.68
0.04	1.46 ± 0.27	0.25 ± 0.10	8.76 ± 1.62
0.03	1.13 ± 0.12	0.10 ± 0.03	6.78 ± 0.72

Table 4.5: Means and standard deviations of the values of the constants c_1 and c_3 in Eq. (3.3) and E in Eq. (4.26), identified in [4] when fitting measurements on polyacrylamide gels (PAG) made with 10% of acrylamide and varying concentrations of bis-acrylamide $[Bis]$.

In experimental observations [2, 14] the substrate is treated as a linear elastic material with Young modulus varying from 1 kPa to 30 kPa. Then, a reasonable choice to compare the different behaviours is to consider the second row of Table 4.5 and assume $c_1 = 2.48$ kPa and $c_3 = 2.50$ kPa for the non-linear response, and $E = 14.88$ kPa for the linear response.

For what concerns the manipulation of the substrate, we refer to the surface load defined in Eq. (3.7) and we consider the circle \mathcal{D} placed in the center of Ω and with radius $23.33 \mu\text{m}$, pulled upwards ($\beta = \pi/2$). About the force magnitude f_b , we do not have in literature a precise value for the manipulation with a microneedle as in [2]. If we assume this value to be close to the *cell traction force* exerted on the substrate in response to the tension applied, a reasonable choice from [2] is $f_b = 6.1$ kPa. The stress, displacement and

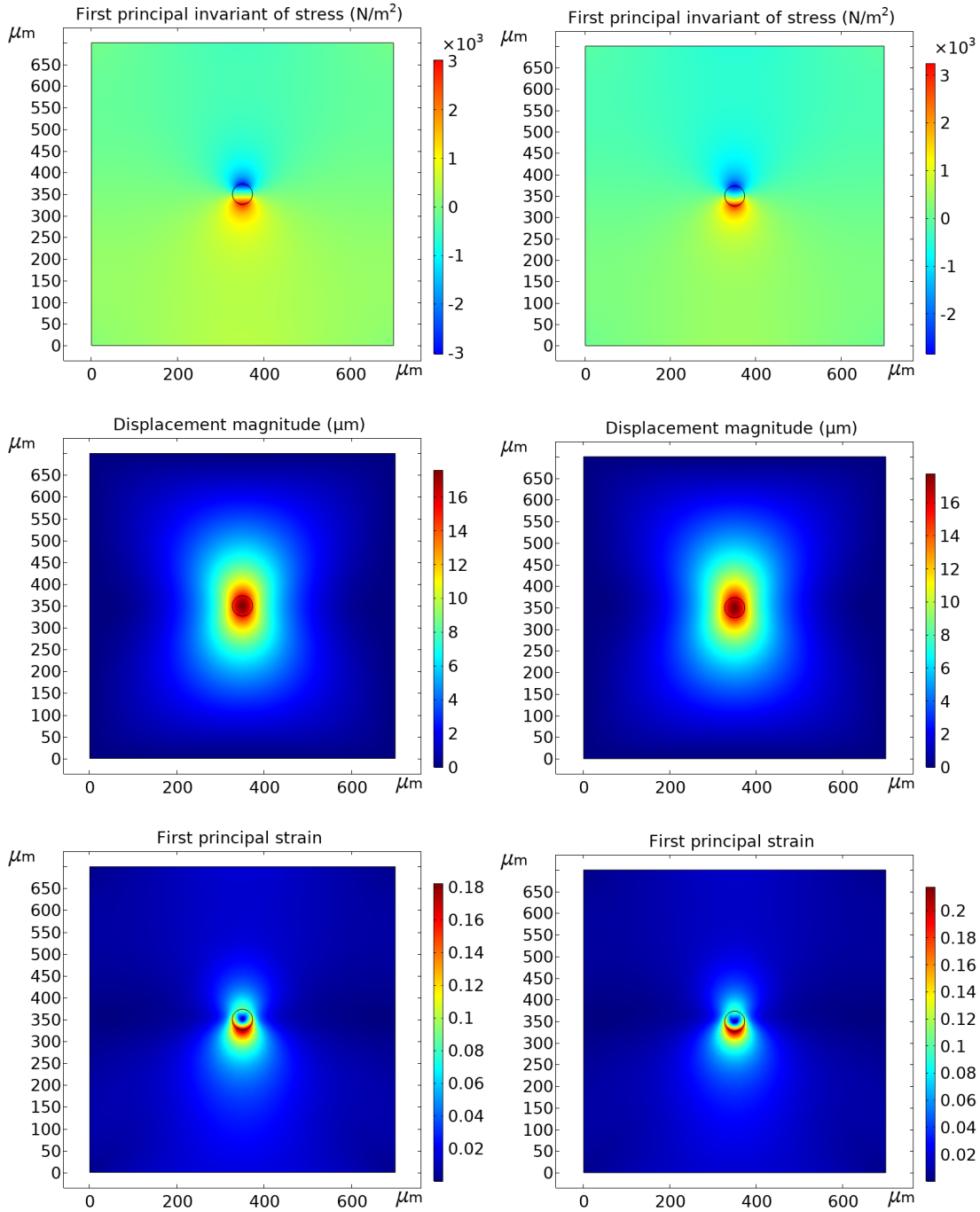


Figure 4.14: Results from the mechanical problem of the substrate, with load in Eq. (3.7) identified by $f_b = 6.1 \text{ kPa}$, $\beta = \pi/2$, and being \mathcal{D} placed in the center of Ω and with radius $23.33 \mu\text{m}$. The left and right columns refer to a linear or non-linear response, respectively.

Mechanical response	$\max I_1$ (kPa)	$\max \mathbf{u} $ (μm)	$\max \lambda_1^{\mathbb{E}}$
Linear	3.03	17.6	0.18
Non-linear	3.25	17.8	0.22

Table 4.6: Maximum values of first principal invariant of stress, displacement magnitude and first principal strain (that is the trace of \mathbb{E}), referring to the results of Fig. 4.14.

strain fields, solutions of both mechanical problems, are shown in Fig. 4.14. Qualitatively, the results are similar; the maximum values are reported in Table 4.6.

Although the results are similar, we mainly notice two issues:

- the maximum displacement magnitude can be compared to the radius of the cell sensing region (20 μm), and this confirms the necessity to display the fields in Eulerian coordinates for the cell migration model;
- in the linear case, we expected small values of displacement and strain, in order to be consistent with the hypothesis of Subsection 2.2.2, but a value 0.18 in strain is too high to be included in a small strain regime. Furthermore, if we take a value of f_b close to the one considered in [4], in which an aspirations of PAG were performed with a micropipette, we may assume $f_b = 15.7$ kPa. In this case the maximum values are shown in Table 4.7, and the necessity for a non-linear response within these loads and stiffnesses is much more evident.

Mechanical response	$\max I_1$ (kPa)	$\max \mathbf{u} $ (μm)	$\max \lambda_1$
Linear	7.80	45.3	0.47
Non-linear	8.69	42.9	0.49

Table 4.7: Maximum values of first principal invariant of stress, displacement magnitude and first principal strain, referring to the same problem of Fig. 4.14, but considering $f_b = 15.7$ kPa.

Taking all these considerations into account, in the following we will assume a non-linear behaviour of the substrate when deformed, even if for smaller loads or higher stiffnesses a linear response could be considered.

4.4.2 Pulling or pushing the substrate

We consider now the same mechanical problem discussed in the previous Subsection (with $f_b = 6.1$ kPa) and simulate the cell migration process. The first principal invariant of stress and the square root of the strain energy density, i.e. the fields c and m , are shown in Eulerian coordinates in Fig. 4.15. For what concerns the choice of the kernel K_θ , the presence of a negative field c leads necessarily to use the “unbiased kernel” as in Eq. (4.4). In fact, with the “biased kernel” as in Eq. (4.3) possible negative values of c in Eq. (3.10)

would bias the cell to reverse its actual direction of polarization at each time t , leading to a null displacement of the cell center or to unstable trajectories, that strongly depend on the numerical method adopted and on the time discretization parameter Δt .

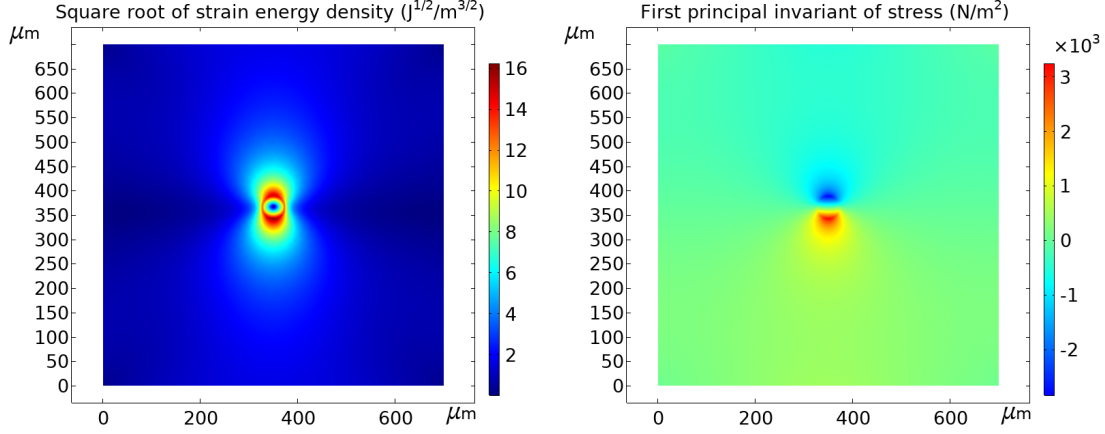


Figure 4.15: The square root of the strain energy density (on the left) and the first principal invariant of stress (on the right) of the substrate, i.e. the fields c and m , are plotted in Eulerian coordinates, for the mechanical problem discussed in Subsection 4.4.1, with $f_b = 6.1$ kPa.

The results presented in this Subsection aim to reproduce qualitatively the experiments of [2] shown in Fig. 1.4, despite the fact that the spatial and temporal scales of the experiment and of our model are not exactly the same.

In Fig. 4.16 and 4.17 we show the trajectories with initial conditions

$$\mathbf{x}_p(0) = (200, 200) \mu\text{m}, \quad \mathbf{w}(0) = (0, -1), \quad (4.27)$$

in order to simulate that the cell is attracted by tensile positive stresses on the substrate, even if it is initially polarized towards a different direction, as in panel (a) of Fig. 1.4.

On the other hand, in Fig. 4.18 and 4.19 we show the trajectories with initial conditions

$$\mathbf{x}_p(0) = (250, 450) \mu\text{m}, \quad \mathbf{w}(0) = (1, 0), \quad (4.28)$$

in order to simulate that the cell is repelled by compressive negative stresses on the substrate, even if it is initially polarized towards a different direction, as in panel (b) of Fig. 1.4. In particular, from the colored symbols of Fig. 4.16 and 4.18 we notice that the cell considerably increases its velocity when it is close to the center of the domain (where the load is applied), as the strain energy reaches its maximum value.

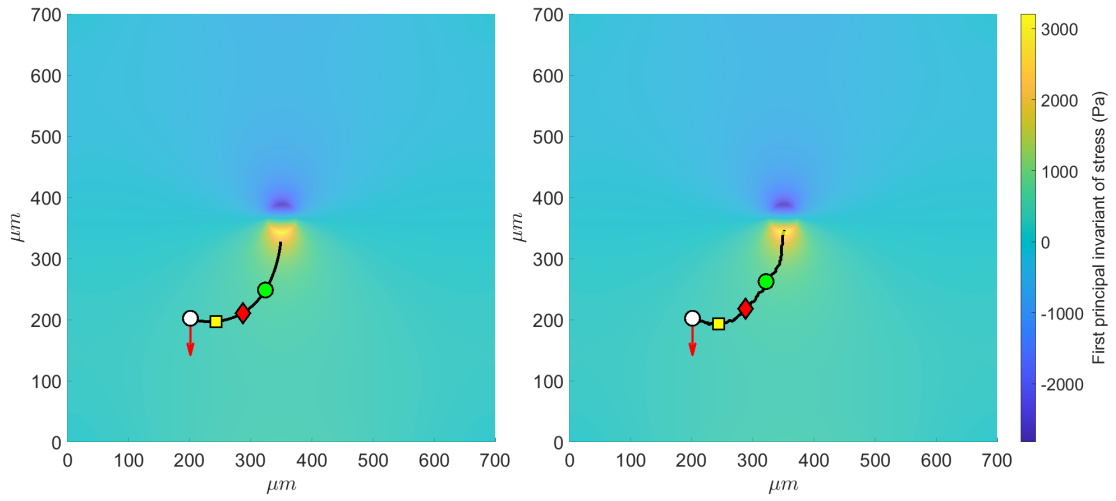


Figure 4.16: Solution with initial conditions set in Eq. (4.27) (white circle and red arrow), computed with $N = 100$ time-steps and $T = 16$ h. The fields c and m are shown in Fig. 4.15. The kernels K_r and K_θ are defined in Eqs. (4.1) and (4.4), respectively. The colored symbols denote the position at the instants $T/4$ (yellow square), $T/2$ (red diamond), $3T/4$ (green circle). On the left, the solution without the random term. On the right, the solution with the additional random term defined in Subsection 4.2.1.

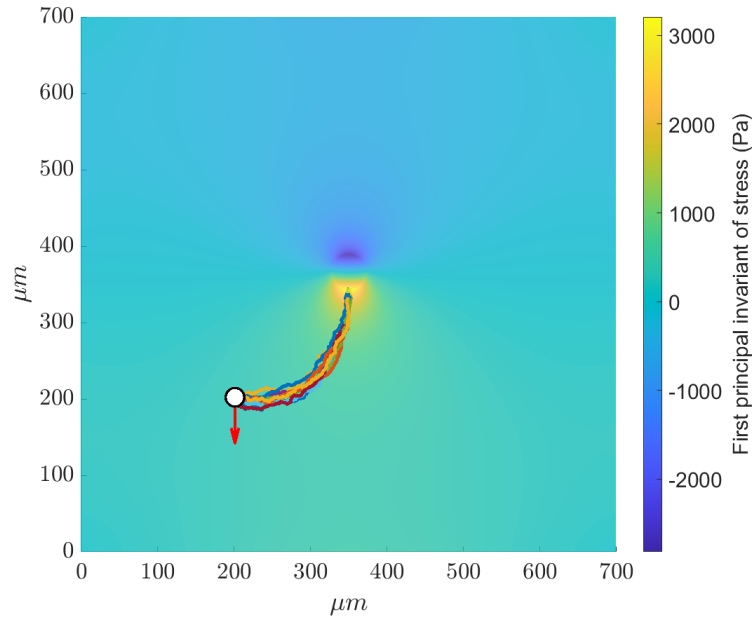


Figure 4.17: 10 different trajectories solutions of the problem set as on the right panel of Fig. 4.16.

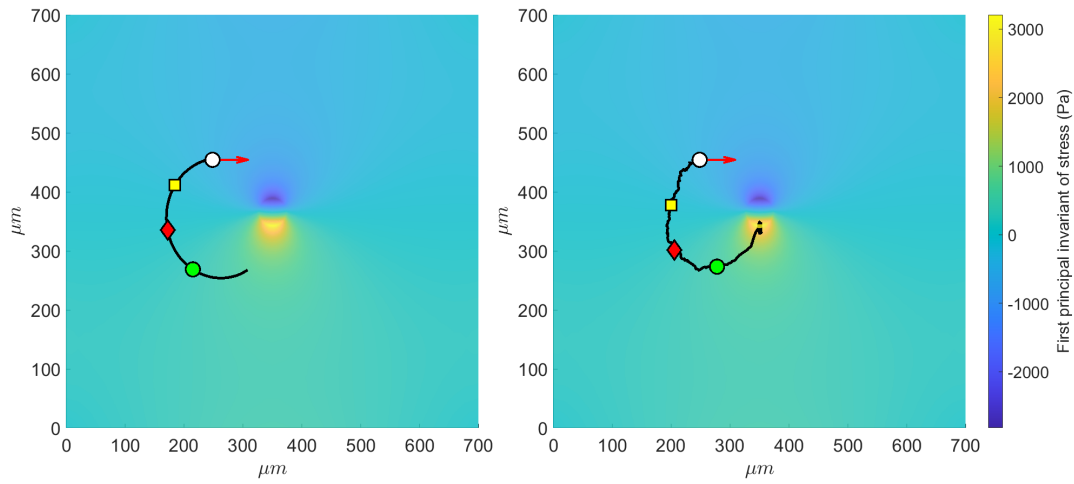


Figure 4.18: Solution with initial conditions set in Eq. (4.28) (white circle and red arrow), computed with $N = 200$ time-steps and $T = 32$ h. The fields c and m are shown in Fig. 4.15. The kernels K_r and K_θ are defined in Eqs. (4.1) and (4.4), respectively. The colored symbols denote the position at the instants $T/4$ (yellow square), $T/2$ (red diamond), $3T/4$ (green circle). On the left, the solution without the random term. On the right, the solution with the additional random term defined in Subsection 4.2.1.

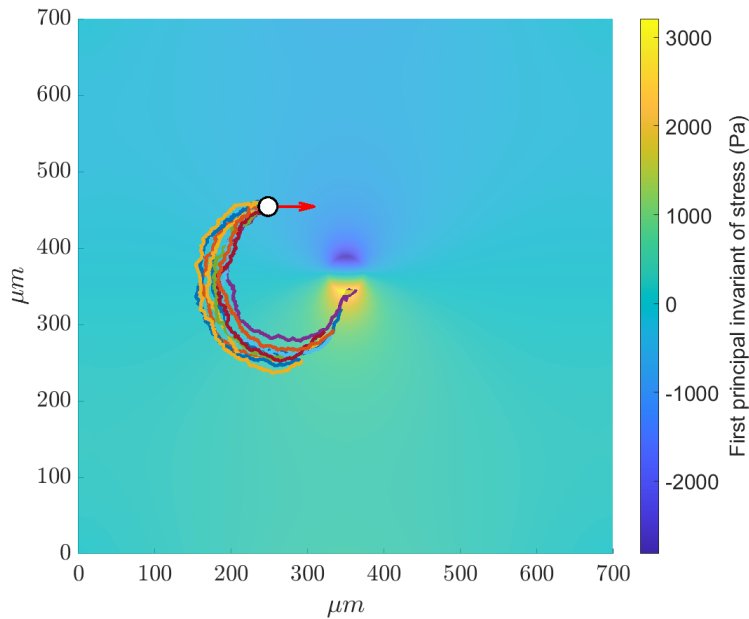


Figure 4.19: 10 different trajectories solutions of the problem set as on the right panel of Fig. 4.18.

Chapter 5

Conclusions and perspectives

Cell migration is essential all along an individual's life, from embryogenesis to tissue repair and cancer metastasis. Thus, due to its biomedical relevance [11, 23], this process is currently under intense research both from the biological and modeling perspectives.

In this dissertation, we have presented a new phenomenological model for cell migration on 2D substrates in response to mechanical stimuli, adapted from the chemotactic model in [1]. In our model a single representative cell changes its motility and its direction of polarization sensing different mechanical cues in a non-local and non-isotropic way through its protrusions in a circular sensing region. We were able to numerically simulate the processes of durotaxis, i.e. the motion towards stiffer regions of the substrate, and tensotaxis, i.e. the motion towards tensile stresses and away from compressive stresses of the substrate itself, and our results qualitatively agree with the experimental observations. We investigated different ways in which the cell can perceive the mechanical cues anisotropically, and we were able to reproduce a typical random Brownian crawling when the cell is not fully polarized. Within the phenomenon of tensotaxis, we showed that a non-linear elastic behaviour of the substrate must be considered in order to deal with all possible mechanical loads found in the literature.

However, our study has many simplifications and limitations, which might be interesting to address in future works. From the modeling point of view, the model is purely phenomenological, and does not take into account the subcellular mechanisms involved in the migration process. In this respect, a multiscale model that succeeds in capturing both levels is certainly a goal, even if, as outlined in Chapter 1, a considerable amount of work has to be done also in understanding the molecular mechanisms involved in the process.

Future works should also focus on the mechanical interaction between the cell and the substrate neglected in the present model. Indeed, we know that cell's mechanical response (elastic or viscoelastic) could also be examined in order to create a more realistic model, since it is known that cells exert traction forces on the substrate they are anchored on [15, 16]. This interaction could be taken into account since it modifies stresses and strains of the substrate itself. This could be captured by our model with the introduction of a mechanical feedback describing forces exchange between the cell and the substrate, since the stress that makes the cell change its polarization and migrate is influenced by the migration process itself. Furthermore, we modeled the substrate

as isotropic. This assumption is true for polyacrylamide gels, but we know that the extracellular matrix may show inhomogeneity and anisotropy [18].

It would be interesting to address time dependent loads and mechanical cues, too. The cell migration model accounts already for possible time dependence of the fields c and m , but a mechanical load that varies over time means a deformation of the substrate that varies over time. This should be addressed within the numerical implementation of the model, since the grid would deform at each different time step. Furthermore, the time interpolation of the fields should be taken into account too, as well as the spatial interpolation already addressed in our model.

Moreover, the simulations we have performed aimed to reproduce the processes of durotaxis and tensotaxis, treating them separately. However, they likely involve similar or analogous subcellular mechanisms and they should be treated congruently and perhaps simulated simultaneously. In general, since cells migrating *in vivo* are exposed to an environment composed of a convolution of biochemical, biophysical, and topological cues, it is likely that cells migrate by performing a sort of “mixotaxis” [48], and it would be interesting to consider more signals in our model, changing properly the fields c and m , or considering different choices of the parameters and of the functions K_r , K_θ and f .

Finally, from the analytical point of view, it would be necessary to investigate more rigorously what a negative field c entails within the existence and uniqueness of the solution, and one could formalize the random term added in Subsection 4.2.1 by writing a proper stochastic differential equation rather than an ODE for Eq. (3.8).

Bibliography

- [1] A. Colombi, S. Falletta, M. Scianna, L. Scuderi (2021), *An integro-differential non-local model for cell migration and its efficient numerical solution*, Mathematics and Computers in Simulation, Vol. 180, 179-204.
- [2] C. Lo, H. Wang, M. Dembo; Y. Wang (2000), *Cell Movement Is Guided by the Rigidity of the Substrate*, Biophysical Journal, Vol. 79, 144–152.
- [3] V. Panzetta, S. Fusco, P. Netti (2019), *Cell mechanosensing is regulated by substrate strain energy rather than stiffness*, Proceedings of the National Academy of Sciences, Vol. 116 (14), 22004-22013.
- [4] T. Boudou, J. Ohayon, C. Picart, R. Pettigrew, P. Tracqui (2009), *Nonlinear elastic properties of polyacrylamide gels: implications for quantification of cellular forces*, Biorheology, Vol. 46 (3), 191-205.
- [5] T. Boudou, J. Ohayon, C. Picart, P. Tracqui (2006), *An extended relationship for the characterization of Young's modulus and Poisson's ratio of tunable polyacrylamide gels*, Biorheology, Vol. 43 (6), 721-728.
- [6] G. Monegato (2008), *Metodi e algoritmi per il calcolo numerico*, Torino, CLUT.
- [7] L. D. Landau, E. M. Lifshitz (1970), *Theory of Elasticity*, 2nd Edition, Moscow, Pergamon Press.
- [8] E. G. Rens, R. Merks (2020), *Cell shape and durotaxis explained from cell-extracellular matrix forces and focal adhesion dynamics*, Iscience, Vol. 23 (9), 101488.
- [9] R. Allena, M. Scianna, L. Preziosi (2016), *A Cellular Potts Model of single cell migration in presence of durotaxis*, Mathematical biosciences, Vol. 275, 57-70.
- [10] Z. Zhang, P. Rosakis, T. Y. Hou, G. Ravichandran (2020), *A minimal mechanosensing model predicts keratocyte evolution on flexible substrates*, Journal of the Royal Society Interface, Vol. 17, 20200175.
- [11] R. Goetzke, A. Sechi, L. De Laporte, S. Neuss, W. Wagner (2018), *Why the impact of mechanical stimuli on stem cells remains a challenge*, Cellular and Molecular Life Sciences, Vol. 75 (18), 3297-3312.
- [12] L. V. Beloussov, N. N. Louchinskaia, A. A. Stein (2000), *Tension-dependent collective cell movements in the early gastrula ectoderm of Xenopus laevis embryos*, Development Genes and Evolution, Vol. 210, 92–104.
- [13] S. V. Plotnikov, A. M. Pasapera, B. Sabass, C. M. Waterman (2012), *Force fluctuations within focal adhesions mediate ECM-rigidity sensing to guide directed cell migration*, Cell, Vol. 151 (7), 1513-1527.
- [14] D. Lachowski, E. Cortes, D. Pink, A. Chronopoulos, S. A. Karim, J. P. Morton,

- E. Armando (2017), *Substrate rigidity controls activation and durotaxis in pancreatic stellate cells*, Scientific reports, Vol. 7 (1), 1-12.
- [15] D. Ambrosi (2006), *Cellular traction as an inverse problem*, SIAM Journal on Applied Mathematics, Vol. 66 (6), 2049-2060.
- [16] R. Merkel, N. Kirchgeßner, C. M. Cesa, B. Hoffmann (2007), *Cell force microscopy on elastic layers of finite thickness*, Biophysical journal, Vol. 93 (9), 3314-3323.
- [17] A. Huttenlocher (2005), *Cell polarization mechanisms during directed cell migration*, Nature cell biology, Vol. 7 (4), 336-337.
- [18] D. K. Schlüter, I. Ramis-Conde, M. A. Chaplain (2012), *Computational modeling of single-cell migration: the leading role of extracellular matrix fibers*, Biophysical journal, Vol. 103 (6), 1141-1151.
- [19] C. Givero, L. Preziosi (2018), *Mechanical perspective on chemotaxis*, Physical Review E, Vol. 98 (6), 062402.
- [20] J. Bueno, Y. Bazilevs, R. Juanes, H. Gomez (2017), *Droplet motion driven by tenso-taxis*, Extreme Mechanics Letters, Vol. 13, 10-16.
- [21] J. Kolega (1986), *Effects of mechanical tension on protrusive activity and microfilament and intermediate filament organization in an epidermal epithelium moving in culture*, The Journal of cell biology, Vol. 102 (4), 1400-1411.
- [22] P. Moreo, J. M. García-Aznar, M. Doblaré (2008), *Modeling mechanosensing and its effect on the migration and proliferation of adherent cells*, Acta biomaterialia, Vol. 4 (3), 613-621.
- [23] N. Wang (2017), *Review of cellular mechanotransduction*, Journal of physics D: Applied physics, Vol. 50 (23), 233002.
- [24] G. De Santis, A. B. Lennon, F. Boschetti, B. Verheghe, P. Verdonck, P. J. Prendergast (2011), *How can cells sense the elasticity of a substrate?: an analysis using a cell tensegrity model*, European cells & materials, Vol. 22, 202-213.
- [25] G. S. Rosalem, E. B. Las Casas, T. P. Lima, L. A. González-Torres (2020), *A mechanobiological model to study upstream cell migration guided by tensotaxis*, Biomechanics and modeling in mechanobiology, Vol. 19 (5), 1537-1549.
- [26] R. Toyozumi, S. Takeuchi (1995), *The behavior of chick gastrula mesodermal cells under the unidirectional tractive force parallel to the substrata*, Journal of cell science, Vol. 108 (2), 557-567.
- [27] S. Forte, L. Preziosi, M. Vianello (2019), *Meccanica dei continui*, Springer.
- [28] S. SenGupta, C. A. Parent, J. E. Bear (2021), *The principles of directed cell migration*, Nature Reviews Molecular Cell Biology, 1-19.
- [29] K. Roberts, B. Alberts, A. Johnson, P. Walter, T. Hunt (2002), *Molecular biology of the cell*, New York: Garland Science, 32(2).
- [30] A. Gagnieu, G. Chagnon, Y. Chemisky, A. Stephanou, A. Chauvière (2019), *On the importance of substrate deformations for cell migration*, Computer Methods in Biomechanics and Biomedical Engineering, Vol. 22, 334-335.
- [31] A. A. Malik, P. Gerlee (2019), *Mathematical modelling of cell migration: stiffness dependent jump rates result in durotaxis*, Journal of mathematical biology, Vol. 78(7), 2289-2315.
- [32] G. Yu, J. Feng, H. Man, H. Levine (2017), *Phenomenological modeling of durotaxis*, Physical Review E, Vol. 96(1), 010402.

-
- [33] A. R. Hassan, T. Biel, T. Kim (2019), *Mechanical Model for Durotactic Cell Migration*, ACS biomaterials science & engineering, Vol. 5(8), 3954-3963.
- [34] COMSOL (2019), *COMSOL Multiphysics: Reference Manual*.
- [35] P. Friedl, D. Gilmour (2009), *Collective cell migration in morphogenesis, regeneration and cancer*, Nature reviews Molecular cell biology, Vol. 10(7), 445-457.
- [36] E. Sahai (2007), *Illuminating the metastatic process*, Nature Reviews Cancer, Vol. 7(10), 737-749.
- [37] E. K. Paluch, I. M. Aspalter, M. Sixt (2016), *Focal adhesion-independent cell migration*, Annual review of cell and developmental biology, Vol. 32, 469-490.
- [38] M. Bergert, A. Erzberger, R. A. Desai, I. M. Aspalter, A. C. Oates, G. Charras, G. Salbreux, E. K. Paluch (2015), *Force transmission during adhesion-independent migration*, Nature cell biology, Vol. 17(4), 524-529.
- [39] M. Abercrombie (1980), *The Croonian Lecture, 1978-The crawling movement of metazoan cells*, Proceedings of the Royal Society of London. Series B. Biological Sciences, Vol. 207(1167), 129-147.
- [40] K. J. Painter (2019), *Mathematical models for chemotaxis and their applications in self-organisation phenomena*, Journal of theoretical biology, Vol. 481, 162-182.
- [41] I. Ramis-Conde, M. A. Chaplain, A. R. Anderson (2008), *Mathematical modelling of cancer cell invasion of tissue*, Mathematical and Computer Modelling, Vol. 47(5-6), 533-545.
- [42] K. Schakenraad, L. Ravazzano, N. Sarkar, J. A. Wondergem, R. M. Merks, M., L. Giomi (2020), *Topotaxis of active Brownian particles*, Physical Review E, Vol. 101(3), 032602.
- [43] N. Ogawa, H. Oku, K. Hashimoto, M. Ishikawa (2006), *A physical model for galvanotaxis of Paramecium cell*, Journal of theoretical biology, Vol. 242(2), 314-328.
- [44] G. Jékely (2009), *Evolution of phototaxis*, Philosophical Transactions of the Royal Society B: Biological Sciences, Vol. 364(1531), 2795-2808.
- [45] A. Galante, S. Wisen, D. Bhaya, D. Levy (2011), *Stochastic models and simulations of phototaxis*, Unifying Themes in Complex Systems, Vol. 8, 105-119.
- [46] H.C. Fu, T. R. Powers, R. Stocker (2012), *Bacterial rheotaxis*, Proceedings of the National Academy of Sciences, Vol. 109(13), 4780-4785.
- [47] K. J. Painter (2021), *The impact of rheotaxis and flow on the aggregation of organisms*, Journal of the Royal Society Interface, 18(183), 20210582.
- [48] E. H. Barriga, E. Theveneau (2020), *In vivo neural crest cell migration is controlled by "Mixotaxis"*, Frontiers in physiology, 1537.
- [49] M. J. Tindall, S. L. Porter, P. K. Maini, G. Gaglia, J. P. Armitage (2008), *Overview of mathematical approaches used to model bacterial chemotaxis I: the single cell*, Bulletin of mathematical biology, Vol. 70(6), 1525-1569.
- [50] M. J. Tindall, S. L. Porter, P. K. Maini, G. Gaglia, J. P. Armitage (2008), *Overview of mathematical approaches used to model bacterial chemotaxis II: bacterial populations*, Bulletin of mathematical biology, Vol. 70(6), 1570-1607..
- [51] E. F. Keller, L. A. Segel (1971), *Model for chemotaxis*, Journal of theoretical biology, 30(2), 225-234.
- [52] <https://it.mathworks.com/help/matlab/ref/scatteredinterpolant.html>

- [53] T. Bobach, G. Umlauf (2006), *Natural neighbor interpolation and order of continuity*, GI Lecture Notes in Informatics: Visualization of Large and Unstructured Data Sets, 69-86.
- [54] I. Amidror (2002), *Scattered data interpolation methods for electronic imaging systems: a survey*, Journal of electronic imaging, Vol. 11(2), 157-176.